## **SUPPORTING INFORMATION**

# Hydrothermally Stable and Regenerable Molybdenum—Zeolite Catalysts for Non-oxidative Conversion of Methane to Dihydrogen and Ethene

Ángel N. Santiago-Colón<sup>1</sup>, Hien Pham<sup>2</sup>, Ayotunde Alabi<sup>1</sup>, David Hibbitts<sup>1</sup>, Abhaya Datye<sup>2</sup>, and Rajamani Gounder<sup>1</sup>\*

<sup>1</sup>Charles D. Davidson School of Chemical Engineering, Purdue University, 480 Stadium Mall

Drive, West Lafayette, IN 47907, USA

<sup>2</sup>Department of Chemical and Biological Engineering, University of New Mexico, Farris
Engineering Center-Suite 1300, Albuquerque, NM 87131-0001, USA

<sup>\*</sup>Corresponding author. E-mail: rgounder@purdue.edu

# Contents

Section S1. Synthesis of zeolites for methane DHA	S3
1.1 Al-CHA Zeolites	<i>S3</i>
1.2 Nano-CHA Zeolites	S4
1.3 Nanosheet-CHA Zeolites	S4
1.4 Meso-CHA Zeolites	S5
1.5 RTH Zeolites	S5
1.6 AEI Zeolites	S5
Section S2. Characterization methods	S7
Section S3. Methane DHA catalytic measurements and forward rate expression	S10
3.1 Methane DHA kinetic measurements and regeneration protocols	S10
3.2 Hydrothermal aging protocols	S11
3.3 Benzene forward rates expression derivation and kinetic calculations	S11
Section S4. Mo-CHA X-ray absorption spectroscopy (XAS) measurements	S14
Section S5. Methane DHA kinetic measurements on Mo-CHA catalyst	S17
Section S6. Supplemental discussion on benzene diffusion through CHA 8-MR windown estimates of Weisz-Prater criterion	
6.1 Supplemental discussion on zeolite flexibility	S23
6.2 Estimation of benzene diffusion coefficient in CHA zeolites	S24
6.3 Weisz-Prater criterion	S25
Section S7. Characterization of CHA zeolites with varying crystallite size	S27
Section S8. Influence of zeolite support topology on product selectivity during methan	
Section S9. Initial benzene formation rates measured on Mo-meso-CHA during DHA	•
Section S10. Characterization of Mo-Zeolites before and after DHA reaction-regenerate	=
Section S11. High resolution transmission electron microscopy	S40
Section S12. Characterization of RTH and AEI zeolites	S41
Section S13. Methane DHA kinetic data on Mo-RTH and Mo-AEI zeolites	S43
References	S45

# Section S1. Synthesis of zeolites for methane DHA

#### 1.1 Al-CHA Zeolites

Al-CHA zeolites were synthesized adapting methods from Di Iorio et al.¹ using Na⁺ and N,N,N-trimethyl-1-adamantylammonium hydroxide (TMAdaOH, 25 wt.% in water, Sachem) as structure directing agents. First, TMAdaOH and NaOH aqueous solution (10 wt.% made from NaOH (98 wt.%, Alfa Aesar pellets) were mixed with deionized water (18.2 MΩ) for 0.25 h in a perfluoroalkoxy alkane (PFA) container with a Teflon stir bar at ambient temperature. Next, aluminum hydroxide (Al(OH)₃, 98 wt.%, SPI Pharma) was added to the solution and mixed for 0.25-0.5 h until solids were completely dissolved. Ludox HS-40 (40 wt.%, Sigma-Aldrich) was finally added to the solution and homogenized for 2-4 h. The molar composition of the synthesis gel was 1 SiO₂/0.033 Al₂O₃/0.3 TMAdaOH/ 0.2 NaOH/44 H₂O for Al-CHA. The synthesis gel was loaded into Parr reactors and sealed under autogenous pressure, which were then placed in a rotation oven (Yamato DKN-402C) at 433 K for 144 h. Solids were recovered using centrifugation and washed with deionized water until a neutral pH was obtained.

As-synthesized solids were then treated in air (1.67 cm<sup>3</sup> s<sup>-1</sup> g<sup>-1</sup>, Air Zero, Indiana Oxygen) in a muffle furnace to 853 K (0.0167 K s<sup>-1</sup>) for 10 h to remove the occluded organic structure directing agent. NH<sub>4</sub><sup>+</sup> exchange procedures were then performed by contacting the solids with a 1 M NH<sub>4</sub>NO<sub>3</sub> solution in a PFA jar with a stir bar for 24 h at ambient temperature. NH<sub>4</sub><sup>+</sup>-CHA zeolites were washed with deionized water and placed overnight in a drying oven at 363 K.

## 1.2 Nano-CHA Zeolites

Nano-CHA zeolites were synthesized by adapting methods from Kumar et al.,<sup>2</sup> using Na<sup>+</sup> and TMAdaOH as the structure directing agents and polyethylenime (PEIM, 50 wt.% in water, Sigma-Aldrich) as the organic surfactant growth modifier. Similar to the synthesis of Al-CHA, the structure directing agents and PEIM were first dissolved in deionized water and homogenized for 2 h followed by addition of aluminum hydroxide (Al(OH)<sub>3</sub>, 98 wt.%, SPI Pharma). Ludox HS-40 (40 wt.%, Sigma-Aldrich) was finally added to the solution and homogenized for 2-4 h. The molar composition of the synthesis gel was 1 SiO<sub>2</sub>/0.033 Al<sub>2</sub>O<sub>3</sub>/0.3 TMAdaOH/ 0.2 NaOH/44 H<sub>2</sub>O and the amount of PEIM added was 1.6 wt.%. The synthesis gel was loaded into Parr bombs and placed in a rotating oven at 433 K for 144 h. Procedures to remove organic content and NH<sub>4</sub><sup>+</sup> exchange were the same used for Al-CHA.

## 1.3 Nanosheet-CHA Zeolites

Nanosheet-CHA zeolites were synthesized by using Na<sup>+</sup> and TMAdaOH as the structure directing agents and dimethyloctadecyl[3-(trimethoxysilyl)propyl]ammonium chloride (TPOAC, 42 wt.% in methanol, Sigma-Aldrich) as the organic surfactant growth modifier.<sup>3</sup> Similar to the synthesis of Al-CHA, the structure directing agents were first dissolved in deionized water and homogenized for 2 h followed by addition of aluminum hydroxide (Al(OH)3, 98 wt.%, SPI Pharma). Ludox HS-40 (40 wt.%, Sigma-Aldrich) was mixed in a separate PFA jar with TPOAC and then added to the synthesis gel, which was homogenized for 24 h before placing in a rotating oven at 433 K for 144 h. The final molar composition of the synthesis gel was 0.033 Al<sub>2</sub>O<sub>3</sub>/0.96 SiO<sub>2</sub>/0.04 TPOAC/0.25 NaOH/0.25 TMAdaOH/44 H<sub>2</sub>O. Procedures to remove organic content and NH<sub>4</sub><sup>+</sup> exchange were the same used for Al-CHA.

#### 1.4 Meso-CHA Zeolites

Mesoporous CHA zeolites (meso-CHA) were synthesized by using Na<sup>+</sup> and TMAdaOH as the structure directing agents and dimethyloctadecyl[3-(trimethoxysilyl)propyl]ammonium chloride (TPOAC, 42 wt.% in methanol, Sigma-Aldrich) as the organic surfactant growth modifier.<sup>3</sup> Similar to the synthesis of Al-CHA, the structure directing agents were first dissolved in deionized water and homogenized for 2 h followed by addition of aluminum hydroxide (Al(OH)<sub>3</sub>, 98 wt.%, SPI Pharma). Fumed silica (Cab-O-Sil M5, Sigma-Aldrich) was mixed in a separate PFA jar with TPOAC and then added to the synthesis gel, which was homogenized for 24 h before placing in a rotating oven at 433 K for 144 h. The final molar composition of the synthesis gel was 0.033 Al<sub>2</sub>O<sub>3</sub>/0.96 SiO<sub>2</sub>/0.04 TPOAC/0.25 NaOH/0.25 TMAdaOH/44 H<sub>2</sub>O. Procedures to remove organic content and NH<sub>4</sub><sup>+</sup> exchange were the same used for Al-CHA.

## 1.5 RTH Zeolites

RTH zeolites were synthesized using the procedure adapted and described by Schmidt et al., using pentamethylimidazolium as the organic structure agent and  $NH_4^+$ -Y zeolite (CBV 720, Zeolyst, Si/Al = 15) as the aluminum and the silica source.

### 1.6 AEI Zeolites

AEI zeolites were synthesized using the procedure adapted and described by Boruntea et al.,<sup>5</sup> using 1,1,3,5-tetramethylpiperidinium hydroxide (35 wt.% in H<sub>2</sub>O, Sachem) as the organic structure agent (OSDA) and NH<sub>4</sub><sup>+</sup>-Y zeolite (CBV 720, Zeolyst, Si/Al = 15) as the aluminum and

the silica source. The final molar composition in the synthesis gel was 1 SiO<sub>2</sub>/0.045 Al<sub>2</sub>O<sub>3</sub>/0.2 OSDA/ 0.2 NaOH/15 H<sub>2</sub>O. Synthesis gels were homogenized for 2 h before being loaded into 45 ml Teflon liners, which were then put inside Parr bombs, sealed under autogenous pressure, and placed into a static oven (Yamato DKN-402C) at 408 K for 7 days.

### Section S2. Characterization methods

Powder X-ray diffraction (XRD) was used to determine zeolite frameworks using an Anton Paar XRDynamic 500 diffractometer with Cu K $\alpha$  radiation source. Samples were loaded in a sample holder with zero background insert (Anton Paar). XRD patterns were collected over a range of 4-40° 20 with a scan rate of 0.0001 s<sup>-1</sup> and are normalized to the highest intensity on each pattern.

Micropore volumes of synthesized zeolites were calculated from Ar adsorption isotherms (87 K) using a Micromeritics 3Flex Adsorption Analyzer. Around 0.03–0.05 g of sample were degassed by heating under vacuum for 2 h at 393 K followed by heating to 623 K for 9 h. The minimum of the plot of  $\partial V_{Adsorbed}/\partial (ln(P/P_0))$  vs  $ln(P/P_0)$  was used to estimate the micropore volume.

Elemental analysis of Mo-zeolites were performed by inductively coupled plasma optical emission spectrometry (ICP-OES) using a Thermo Scientific iCAP 7000 Plus Series ICP-OES. Samples (0.02–0.03) were digested in 2.5 g of hydrofluoric (HF) acid (48 wt.%, TraceMetal Grade, Fischer Chemical) for 48 h followed by addition of 50 g of deionized water (18.2 MΩ). For ICP-OES analysis around 0.3 g of HNO<sub>3</sub> (70 wt.%, Sigma-Aldrich) were added to 10 g of digested sample solution.

H<sub>2</sub> temperature programmed reduction (H<sub>2</sub> TPR) was performed using a Micromeritics Autochem II 2920 equipped with a thermal conductivity detector (TCD). Samples (0.04–0.06 g) were loaded into a U-tube quartz reactor and supported between two quartz wool plugs (Fischer Scientific). Before each experiment, Mo-zeolites were pretreated under flowing air (0.5 cm<sup>3</sup> s<sup>-1</sup>, Air Zero, Indiana Oxygen) at 823 K (0.167 K s<sup>-1</sup>) for 3 h followed by cooling down to 353 K. Then, a stream of 5% H<sub>2</sub> in balance Ar (Certified Mixture, Indiana Oxygen) was sent through the

sample until a stable TCD baseline was obtained (~0.5 h). Temperature was then ramped to 900 K (0.167 K s<sup>-1</sup>, hold 1 h) followed by a second temperature ramp to 1273 K (0.167 K s<sup>-1</sup>, hold 0.25 h). A slurry mixture of 2-propanol (Sigma Aldrich, 99.5%) and liquid N<sub>2</sub> was placed after the TPR reactor (and upstream of the TCD) to condense water formed during the reduction process. TPR profiles were baseline corrected, and a response factor was generated (to enable quantification of H<sub>2</sub> consumed) by diluting a 5% H<sub>2</sub> (in balance Ar, Certified Mixture, Indiana Oxygen) stream with Argon (UHP, 99.999%, Indiana Oxygen). The response factor was adjusted by performing a TPR using Ag<sub>2</sub>O standard (Micromeritics) such that the consumed H<sub>2</sub>/Ag<sub>2</sub>O ratio is equal to the value specified by vendor (0.99).

Ammonia gas titration methods for quantifying residual H<sup>+</sup> sites on Mo-MFI and Mo-CHA materials were adapted from our previous work<sup>6</sup> and performed using a Micromeritics Autochem II 2920 connected to a residual gas analyzer (MKS Cirrus). Before each measurement, an NH<sub>3</sub> response factor was generated by diluting the stream of gaseous NH<sub>3</sub> (500 ppm in balance He, Certified Mixture, Indiana Oxygen) with He (0.833 cm<sup>3</sup> s<sup>-1</sup>, UHP, 99.999%, Indiana Oxygen). Around 0.04–0.05 g of sample was supported between two quartz wool plugs (Fischer Scientific) in a U-tube quartz reactor and pretreated under flowing air (0.833 cm<sup>3</sup> s<sup>-1</sup>, Air Zero, Indiana Oxygen) at 823 K (0.167 K s<sup>-1</sup>) for 2 h. Then a stream of gaseous NH<sub>3</sub> (0.833 cm<sup>3</sup> s<sup>-1</sup>) was flown to the sample for 2 h at 433 K followed by flowing wet (1-2 kPa H<sub>2</sub>O) He (0.833 cm<sup>3</sup> s<sup>-1</sup>) at 433 K for 20 h to desorb Lewis-bound NH<sub>3</sub> from Mo species and extra-framework Al species. Desorption of NH<sub>3</sub> was performed by ramping the temperature from 433 K to 873 K (0.167 K s<sup>-1</sup>, 0.5 h hold).

Transmission electron microscopy (TEM) images were collected in a JEOL NEOARM 200CF microscope equipped with spherical aberration correction to allow atomic resolution

imaging. Samples were dispersed in ethanol and mounted on lacey carbon grids for examination. Images were recorded simultaneously in annular dark field (ADF)-STEM and annular bright field (ABF)-STEM modes, and in high-resolution TEM (HRTEM) mode.

In situ X-ray absorption spectroscopy (XAS) experiments were conducted at the Advanced Photon Source at Argonne National Laboratory (Sector 10-BM) and at Brookhaven National Laboratory (BNL, Sector 8-ID). Various reference Mo compounds with were analyzed to generate a response between X-ray absorption near edge structure (XANES) and oxidation state: Mo trioxide (MoO<sub>3</sub>, 99.97%, Sigma Aldrich), sodium molybdate (Na<sub>2</sub>MoO<sub>4</sub>, ≥98%, Sigma Aldrich) molybdenum dioxide (MoO2, 99%, Thermo Fischer Scientific), molybdenum acetate (C<sub>8</sub>H<sub>12</sub>Mo<sub>2</sub>O<sub>8</sub>, 98.8%, Thermo Fischer Scientific) and molybdenum carbide (Mo<sub>2</sub>C, 325 Mesh, 99.5%, Millipore Sigma). At ANL, samples (0.05–0.15 g) were loaded into a six-shooter that was placed on a Kapton-sealed quartz tube. At BNL, samples were loaded into capillary tubes supported by quartz wool plugs and then placed in a custom-built cell with heating elements surrounding the reactor setup. Reference compounds were scanned at ambient temperature while Mo-Zeolite were treated in various gas environment (e.g., 20 kPa O<sub>2</sub> in balance He, 60 kPa CH<sub>4</sub> in balance He) and temperatures (473–973 K) and scans were collected in transmission mode at ambient temperature from 0.2 keV below and 0.9 keV above Mo K-edge (20.0000 keV). Data analysis were performed in WinXAS 3.2 software package.

Scanning electron microscopy (SEM) images were collected with a FEI Quanta 3D FEG Dual-beam SEM instrument with an Everhart–Thornley detector operating at 2 keV. Samples were coated with platinum and the spot was chosen to be between  $0.5-3~\mu m$ .

# Section S3. Methane DHA catalytic measurements and forward rate expression

# 3.1 Methane DHA kinetic measurements and regeneration protocols

Methane DHA catalytic measurements were performed on a tubular quartz reactor (12.7 mm ID) connected to a gas chromatograph (GC Agilent 6890) equipped with a capillary column (DB-1, 50 m × 320 μm × 5 μm) connected to a flame ionization detector for quantification of hydrocarbons and a packed column (Supelco 60/80 Carboxen 1000, 4.5 m × 3.2 mm) connected to a TCD for quantification of H<sub>2</sub>, Ar, CO, and CH<sub>4</sub>. A packed pre-column (Supelco 60/80 Carboxen 1000, 1.52 m × 3.2 mm) was placed before the packed column to retain hydrocarbons from TCD analysis and was flushed 0.1 h after each injection.

Mo-zeolites were pelletized and sieved to obtain particles between 180–250 μm. Around 0.3–0.5 g of catalyst was placed between two quartz wool plugs in the tubular reactor. Reactor temperature was controlled using a clam-shell furnace connected to a K-Type thermocouple (Omega) above the catalyst bed. The temperature was increased to 950 K (0.1 K s<sup>-1</sup>) under flowing Ar (0.333 cm<sup>3</sup> s<sup>-1</sup>, UHP, Indiana Oxygen) and held for 0.5–1 h. Then, a gas stream of 90/10 (v/v %) CH<sub>4</sub>/Ar (0.25 cm<sup>3</sup> s<sup>-1</sup>, Certified Gravimetric Mixture, Indiana Oxygen) was introduced to the reactor to start the reaction followed by first injection at 0.0833 h. The reaction was carried out until catalyst deactivated to 80–90% of the initial benzene formation rate. The regeneration protocol consisted in cooling down the catalyst to 823 K under flowing Ar (hold 0.5 h) before introducing a stream of air (0.2 cm<sup>3</sup> s<sup>-1</sup>, Air Zero, Indiana Oxygen) for >6 h. After regeneration, the temperature was ramped (0.167 K s<sup>-1</sup>) under flowing Ar to reaction temperature (950 K) to start the subsequent reaction-regeneration cycle.

# 3.2 Hydrothermal aging protocols

First, methane DHA kinetic measurements were performed on fresh catalysts (Mo-MFI, Mo-nanosheet-CHA); we denote this measurement to Cycle 1. The reactor with the spent catalyst was then placed inside a ceramic furnace (Watlow) where temperature was controlled by a K-Type thermocouple (Omega) external to the catalyst bed. The temperature was increased to 923 K (0.083 K s<sup>-1</sup>) under flowing He (1.67 cm<sup>3</sup> s<sup>-1</sup>, UHP, 99.999%, Indiana Oxygen) and held for 20 min. Next, water (18.2 M) was introduced via syringe pump (KDS Legato 100 Series, KD Scientific) at a rate of 4.7 μL min<sup>-1</sup> in flowing air (1.67 cm<sup>3</sup> s<sup>-1</sup>, Air Zero, Indiana Oxygen) to prepare a stream with ~20 kPa H<sub>2</sub>O, which was then flown to the spent catalysts for 8 h. Upstream and downstream transfer lines in the reactor were heated to >393 K to prevent water condensation. The reactor was then placed in the methane DHA unit for kinetic measurements. The HTA regeneration was repeated 2 times for both catalysts (i.e., total of 3 cycles).

## 3.3 Benzene forward rates expression derivation and kinetic calculations

Benzene forward rates were determined using the expression derived from Razdan et al. Complete derivation and assumptions can be found in literature.<sup>8</sup> For this work, we used the following expression:

$$\vec{R} = \frac{\langle R \rangle}{1 - z_{Ov}^{1/\bar{\sigma}}} \tag{S1}$$

where  $\langle R \rangle$  is the net rate normalized by moles of Mo,  $z_{0v}$  is the overall approach to equilibrium, and  $\bar{\sigma}$  is the affinity-averaged stoichiometric number. The reactor used for methane DHA is not considered a differential reactor, since there are concentration gradients through the length of the

reactor. Thus, the net rate is defined considering the products (i.e., naphthalene) that are presumably formed from benzene:

$$\langle R \rangle = F_{C_6 H_6} + F_{C_{10} H_6}$$
 (S2)

where  $F_i$  is the molar flowrate of benzene and naphthalene normalized by moles of Mo. Moreover,  $z_{Ov}$ , the overall approach to equilibrium is defined as:

$$z_{Ov} = \frac{P_{C_6 H_6} P_{H_2}^9}{P_{CH_4}^6 K_{eq.}}$$
 (S3)

where the  $K_{eq}$  is the equilibrium constant determined at 950 K for the methane DHA reaction. The affinity-averaged stoichiometric number was determined with the following expression assuming that ethylene is the main intermediate to form benzene:

$$\bar{\sigma} = \frac{\sigma_A^* \ln z_A^* + \sigma_B^* \ln z_B^* + \sigma_C^* \ln z_C^*}{\ln z_A^* + \ln z_B^* + \ln z_C^*}$$
(S4)

where A, B, and C are elementary steps proposed by Razdan et al.,  $\sigma_i^*$  is the stoichiometric number of rate determining step of global phase step i, and  $z_i^*$  is the gas-phase global approach to equilibrium of i step. Reactions A-C are defined as:

$$A. \ 2CH_4 = C_2H_6 + H_2$$
 (S5)

B. 
$$C_2H_6 \leftrightharpoons C_2H_4 + H_2$$
 (S6)

$$C. 3C_2H_4 = C_6H_6 + 3H_2$$
 (S7)

 $\mathbf{z}_i^*$  is defined for each global phase reaction as:

$$z_A^* = \frac{P_{C_2H_6}P_{H_2}}{P_{CH_4}^2K_{eq.}} \tag{S8}$$

$$z_B^* = \frac{P_{C_2H_4}P_{H_2}}{P_{C_2H_6}K_{eq.}} \tag{S9}$$

$$z_C^* = \frac{P_{C_6H_6}P_{H_2}^3}{P_{C_2H_4}^3K_{eq.}} \tag{S10}$$

The initial reaction time was considered to be the opening of the mass flow controller to introduce the 90/10 vol.% CH<sub>4</sub>/Ar flow to the reactor. For all reactions, the first GC injection was performed at 0.083 h. Argon was used as the internal standard and methane was used to correlate the internal standard from the TCD to the FID. The carbon balance was determined as:

Carbon Balance = 
$$\frac{\sum_{i} n_{i} F_{i}}{F_{CH_{4,in}} - F_{CH_{4,out}}}$$
(S11)

Methane conversion:

$$X_{CH_4} = \frac{F_{CH_{4,in}} - F_{CH_{4,out}}}{F_{CH_{4,in}}}$$
 (S12)

Carbon yield:

$$Carbon Yield = \frac{\sum_{i} n_{i} F_{i}}{F_{CH_{A,in}}}$$
 (S13)

Gas-phase selectivity:

Gas Phase Selectivity = 
$$\frac{n_j F_j}{\sum_i n_i F_i}$$
 (S14)

where  $n_i$  is the number of carbon atoms in i product and  $F_i$  and is the flow rate of i product.

Cumulative production (per Mo) or cumulative turnover number of each species (including dihydrogen) was determined using data measured during time-on-stream:

Cumulative turnover of jth species = 
$$TON_j = \int_0^t F_j dt$$
 (S15)

And the cumulative total carbon products turnover number (TON) is defined as:

$$TON = \sum_{j} TON_{j}$$
 (S16)

# Section S4. Mo-CHA X-ray absorption spectroscopy (XAS) measurements

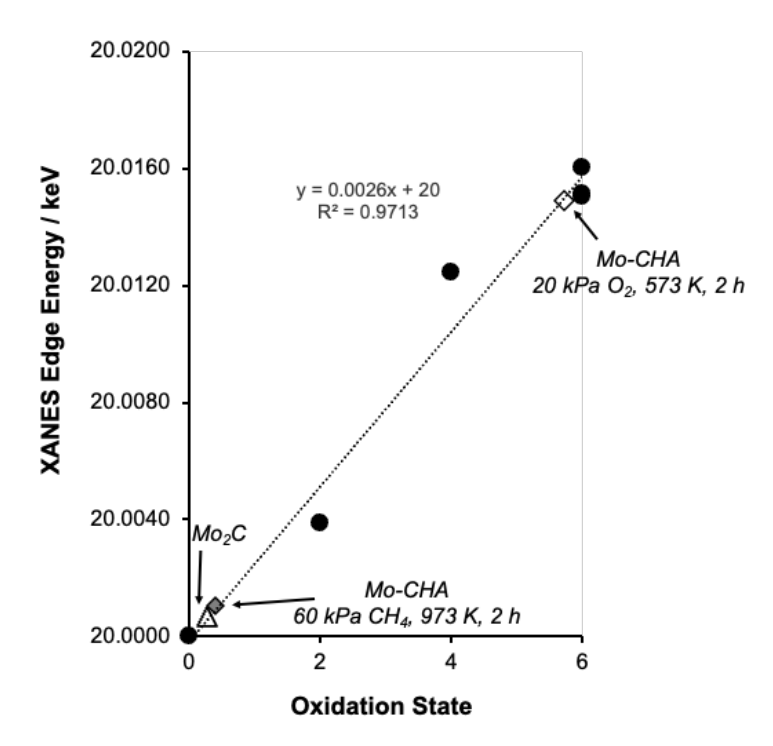


**Figure S1.** XANES edge energy measured on Mo standards (black circles), Mo-CHA (diamonds), and Mo<sub>2</sub>C (triangles). Trendline was fitted to Mo standards to relate oxidation state with edge energy. Data collected at ANL.

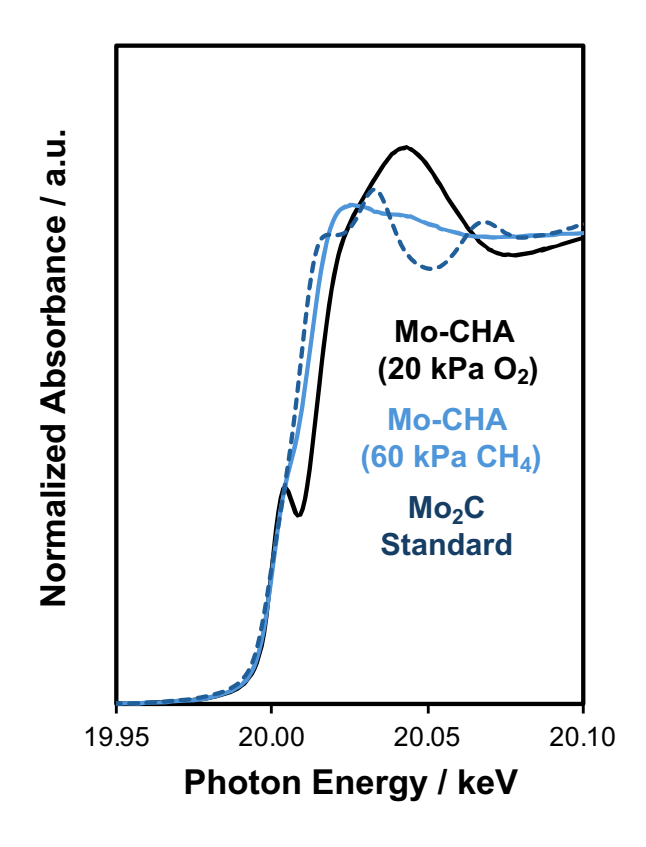


**Figure S2.** Normalized XANES edge energy spectra of Mo-CHA after 20 kPa O<sub>2</sub> treatment at 823 K (black solid line), Mo-CHA after 60 kPa CH<sub>4</sub> treatment at 973 K (blue solid line), and Mo<sub>2</sub>C standard (dark blue dashed line). Data collected at ANL.

Table S1. Edge energy on Mo-CHA after various treatments determined from XANES.

Sample	Treatment	Edge energy / keV
Mo-CHA	20 kPa O <sub>2</sub> , 573 K, 2 h	20.01488
Mo-CHA	60 kPa CH <sub>4</sub> , 973, 2 h	20.00105
$Mo_2C$	None	20.00070

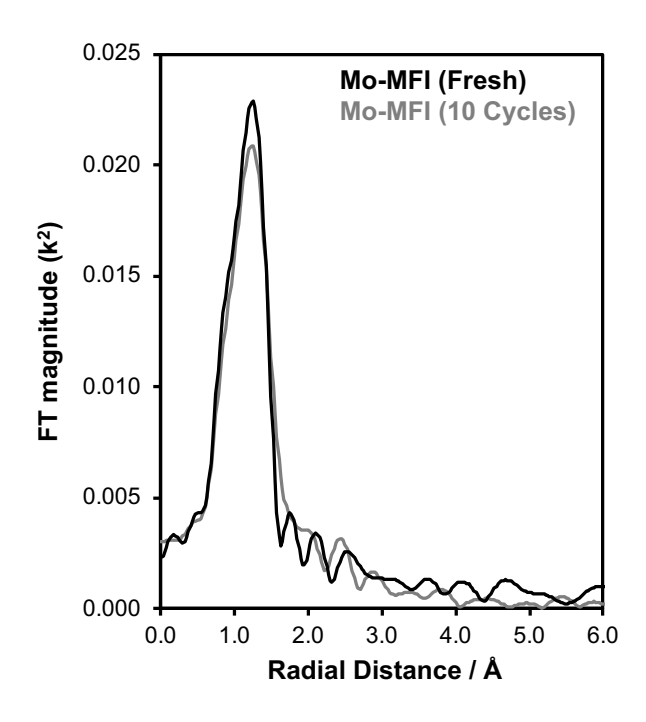


**Figure S3.** EXAFS of fresh Mo-MFI (black trace) and Mo-MFI after 10 reaction-regeneration cycles (grey trace) after 20 kPa O<sub>2</sub> treatment at 823 K. Data collected at BNL.

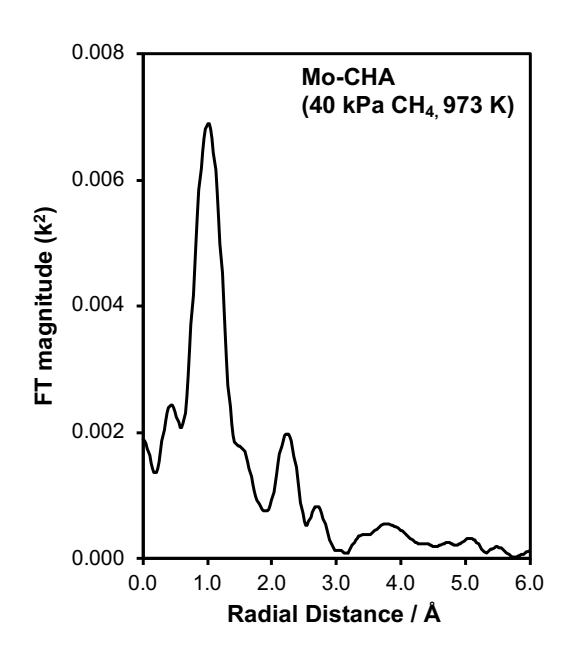
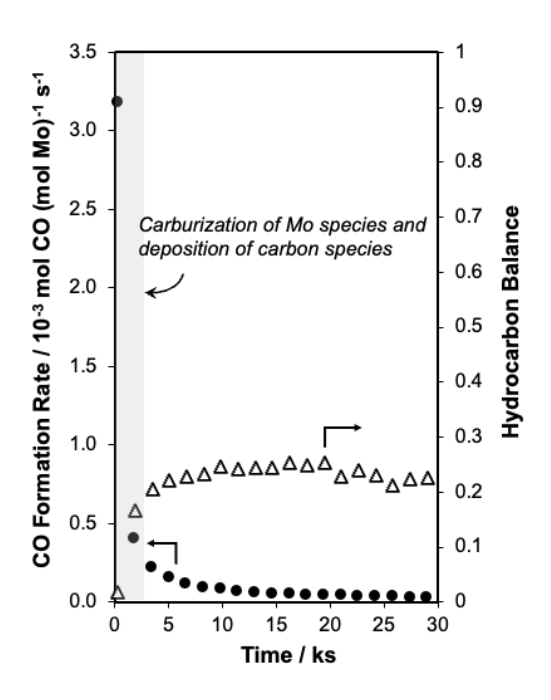


Figure S4. EXAFS of Mo-CHA after 60 kPa CH<sub>4</sub> treatment at 723 K (2 h). Data collected at ANL.

# Section S5. Methane DHA kinetic measurements on Mo-CHA catalyst



**Figure S5.** CO formation rate (per Mo) and hydrocarbon balance during time-on-stream measured on Mo-CHA. Shaded grey area is a visual guide for early (<1 ks) time-on-stream assigned to carburization of ion-exchanged Mo species and deposition of carbonaceous deposits on Mo-CHA. Reaction conditions: 950 K, 90/10 (v/v %) CH<sub>4</sub>/Ar, 110 kPa total pressure, 12.2 mol Mo·s (mol CH<sub>4</sub>)<sup>-1</sup>.

**Table S2.** Benzene forward formation rates (per Mo) measured on Mo-MFI in literature.

Reference	Temperature and Pressure	Benzene forward rate / 10 <sup>-3</sup> mol C <sub>6</sub> H <sub>6</sub> (mol Mo) <sup>-1</sup> s <sup>-1</sup>	Max Hydrocarbon Balance
Bedard et al.9	950 K, 90 kPa	0.43	Not reported
Razdan et al.8	973 K, 90 kPa	0.38	>0.95
Santiago-Colón and Gounder <sup>6</sup>	950 K, 60 kPa	0.54	0.88
This work (Mo-CHA)	950 K, 90 kPa	0.11	0.24

Approach-to-equilibrium values calculated for the initial entry-step reactions in the methane DHA network (i.e., methane-to-ethane and ethane-to-ethene) are equilibrated ( $\eta \sim 0.9$ –1; Supplementary Figure 6) at early times-on-stream, suggesting that methane, ethane, and ethene form a quasi-equilibrated pool, as also observed during methane DHA on Mo-MFI.<sup>8</sup>

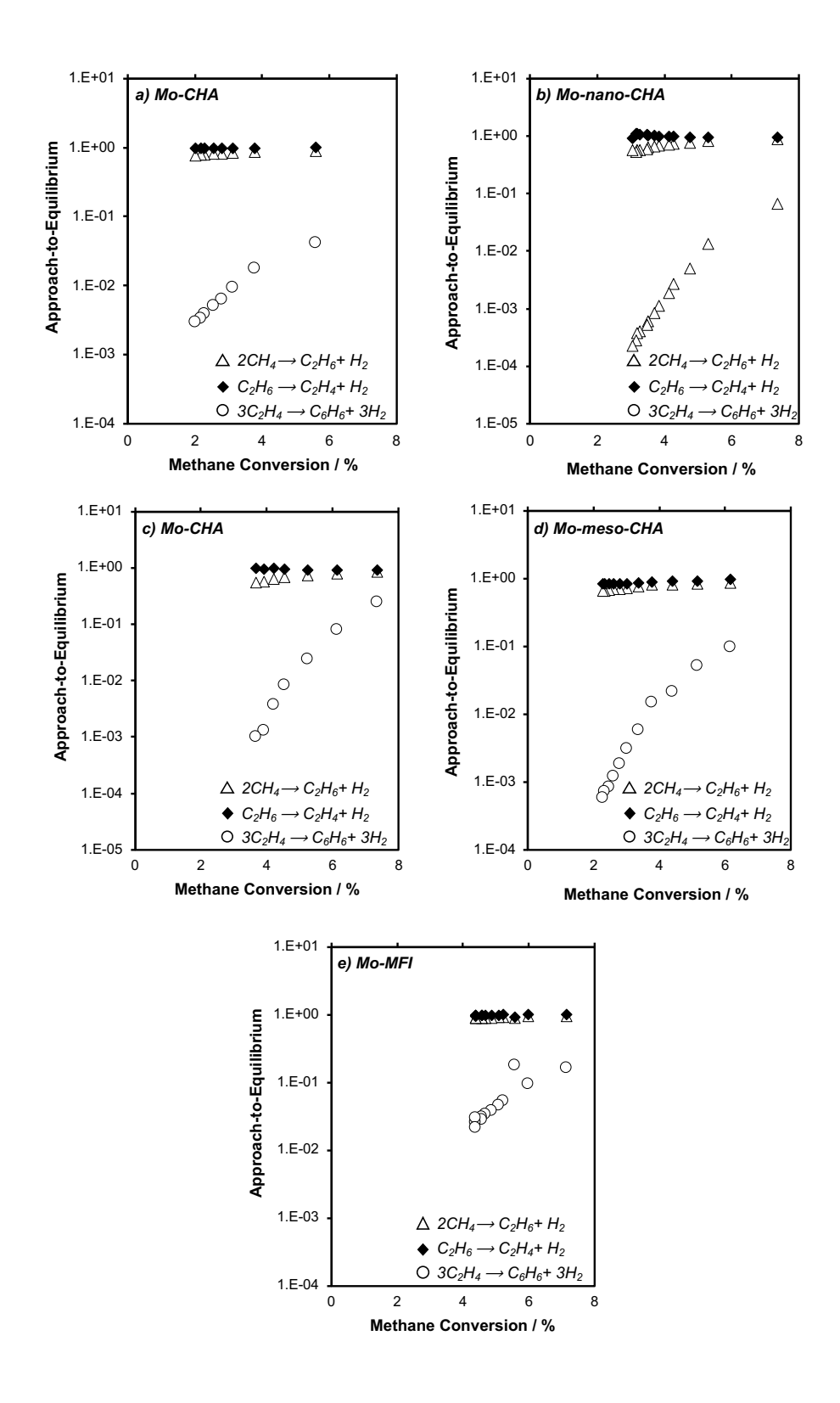


**Figure S6.** Approach-to-equilibrium of methane-to-ethane (open triangles), ethane-to-ethene (black diamonds), and ethene-to-benzene (open circles) reactions measured during deactivation of a) Mo-CHA, b) Mo-nano-CHA, c) Mo-nanosheet-CHA, d) Mo-meso-CHA, e) Mo-MFI catalysts.

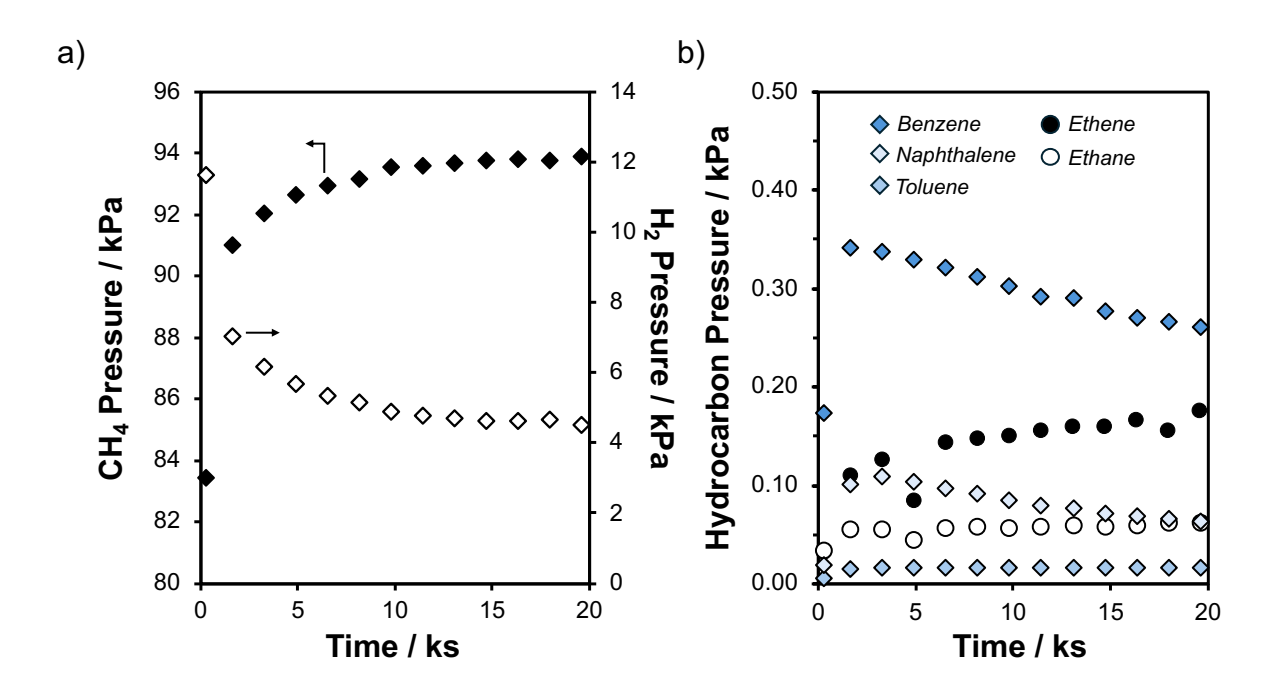


**Figure S7.** Measured outlet partial pressure of a) methane and dihydrogen, and b) ethane, ethene, benzene, toluene, and naphthalene on Mo-MFI.

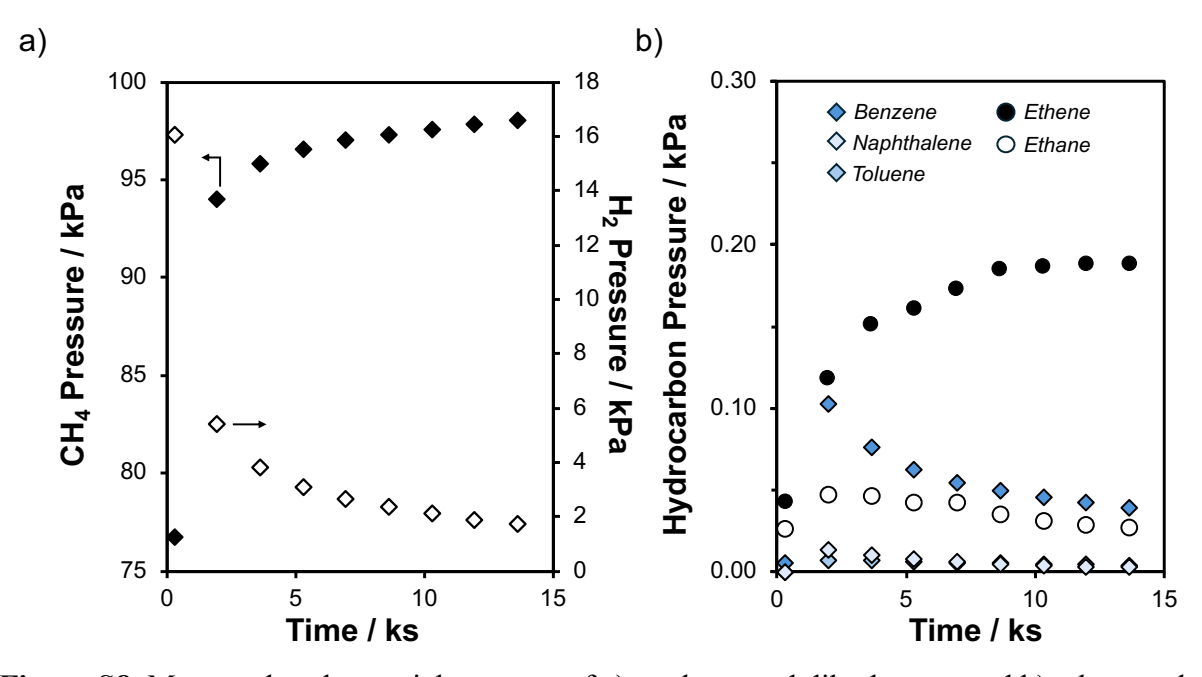


**Figure S8.** Measured outlet partial pressure of a) methane and dihydrogen, and b) ethane, ethene, benzene, toluene, and naphthalene on Mo-CHA.

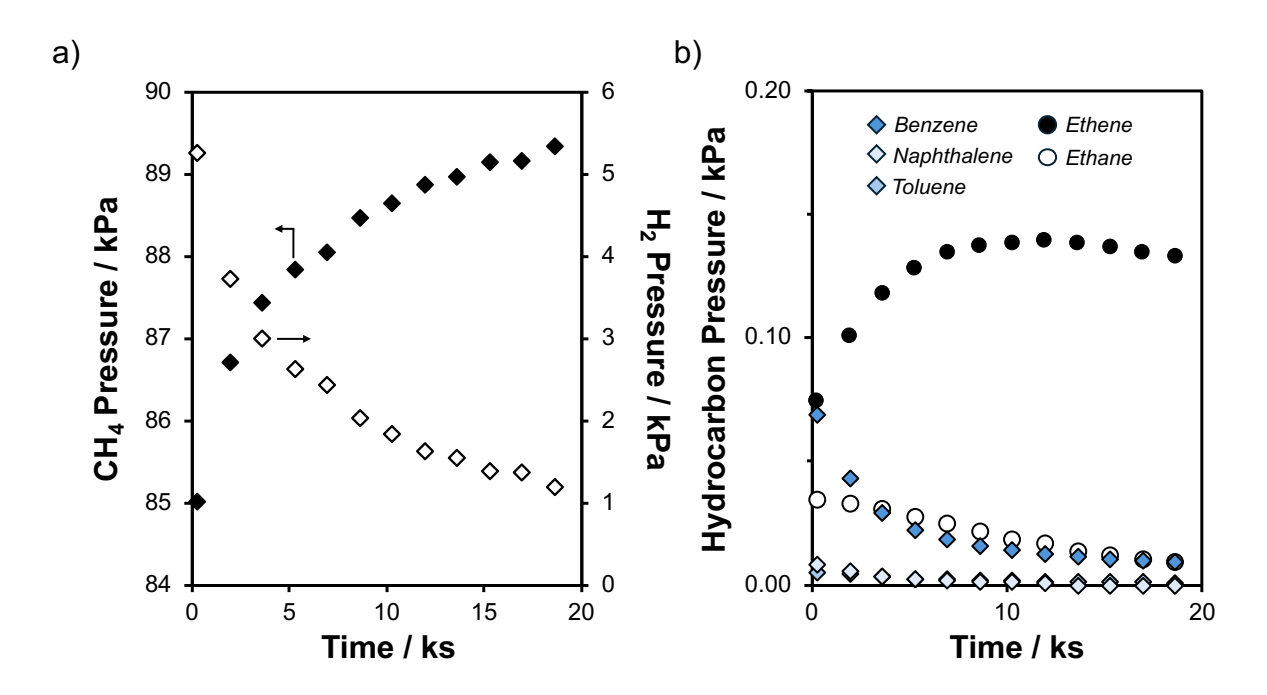


**Figure S9.** Measured outlet partial pressure of a) methane and dihydrogen, and b) ethane, ethene, benzene, toluene, and naphthalene on Mo-nano-CHA.

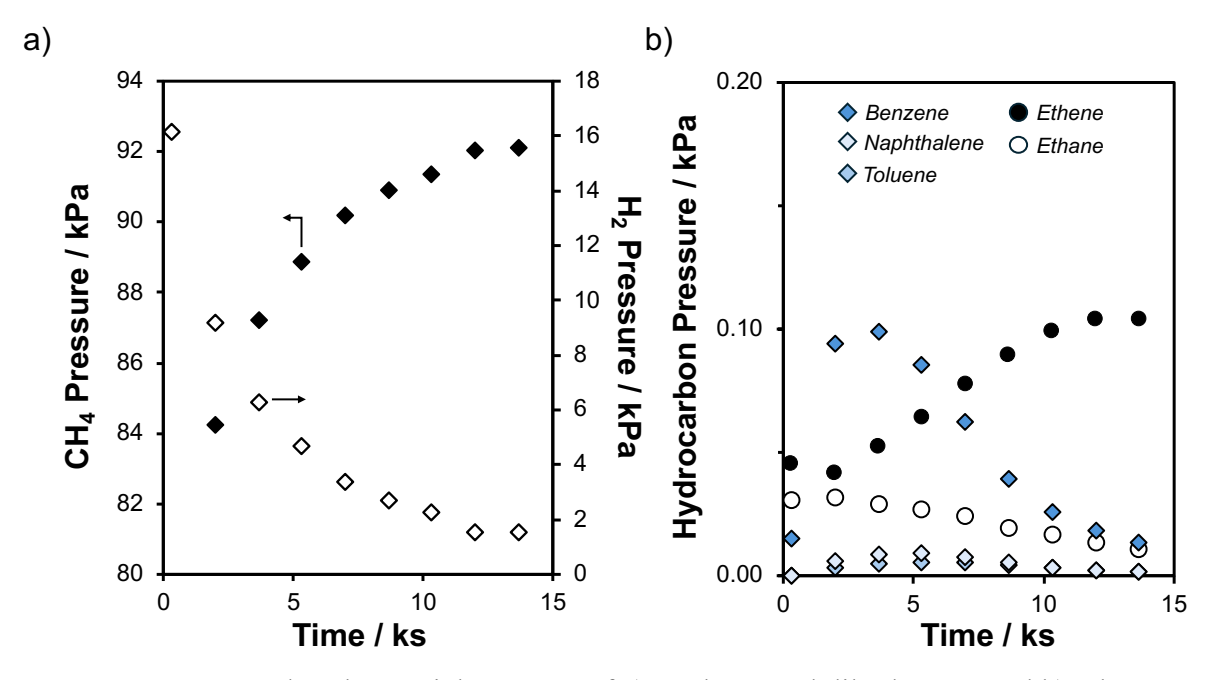


**Figure S10.** Measured outlet partial pressure of a) methane and dihydrogen, and b) ethane, ethene, benzene, toluene, and naphthalene on Mo-nanosheet-CHA.

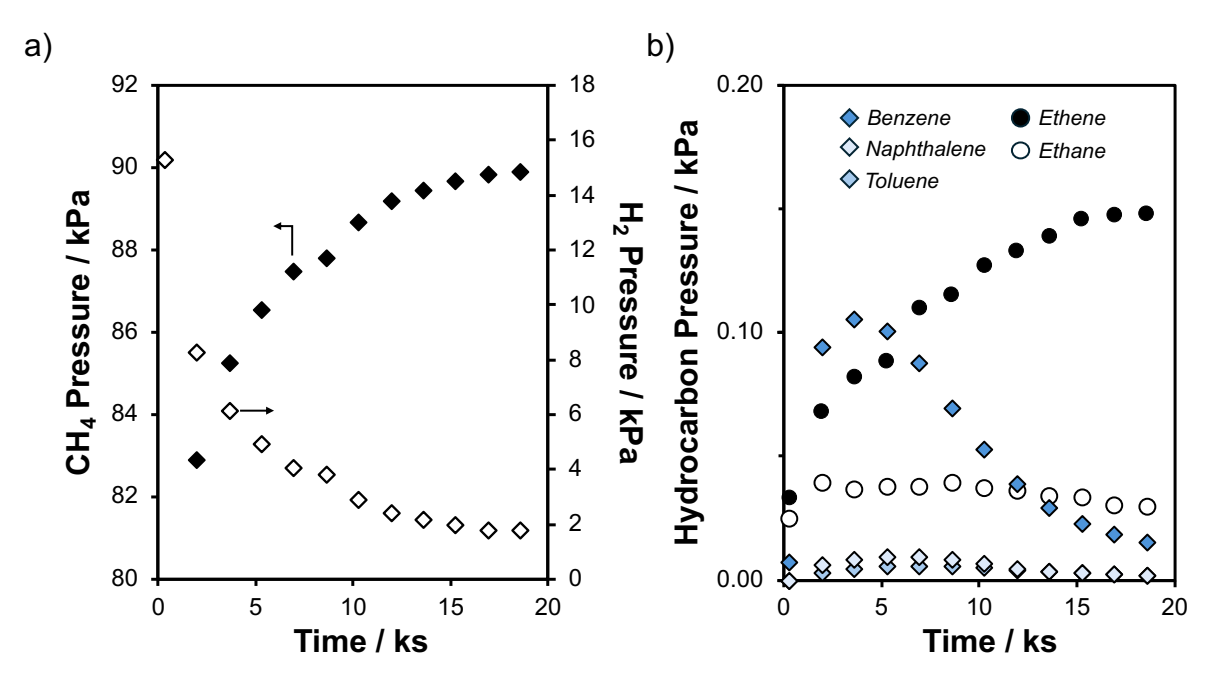


**Figure S11.** Measured outlet partial pressure of a) methane and dihydrogen, and b) ethane, ethene, benzene, toluene, and naphthalene on Mo-meso-CHA.

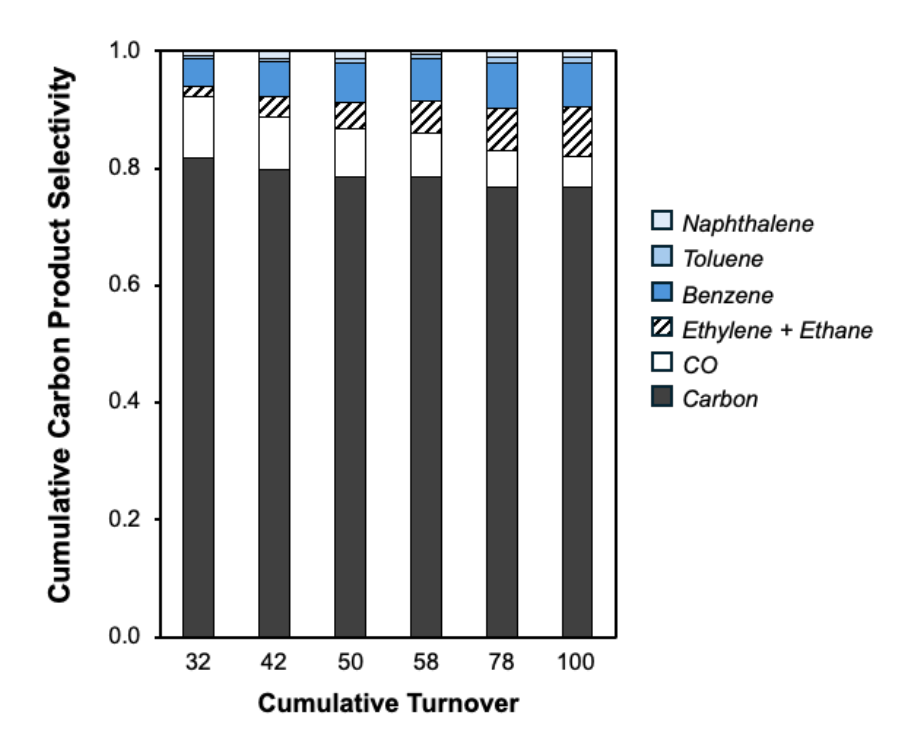


**Figure S12.** Carbon product selectivity as a function of cumulative turnover number. Reaction conditions: 950 K, 90/10 (v/v %) CH<sub>4</sub>/Ar, 110 kPa total pressure, 12.2 mol Mo·s (mol CH<sub>4</sub>)<sup>-1</sup>.

Gas-phase selectivities measured on Mo-CHA and Mo-MFI are compared in Figure S13. Although benzene selectivity is similar in Mo-CHA and Mo-MFI catalysts, naphthalene selectivity is 2–3x lower in Mo-CHA. C<sub>2</sub> species (i.e., ethylene and ethane) gas-phase selectivity is ~5x higher on Mo-CHA compared to Mo-MFI.

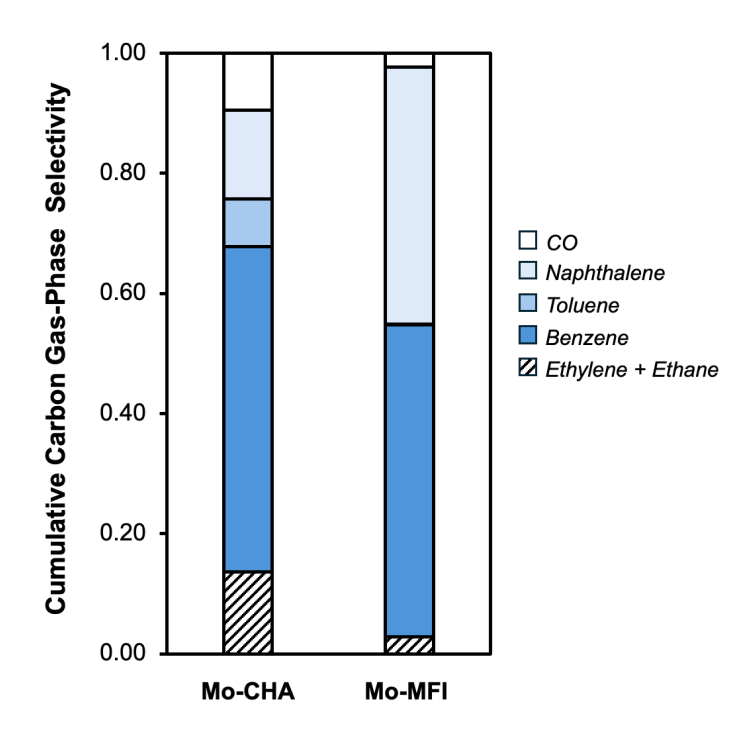


**Figure S13.** Gas-phase product selectivity at ~58 TON measured on Mo-CHA and Mo-MFI catalysts. Reaction conditions: 950 K, 90/10 (v/v %) CH<sub>4</sub>/Ar, 110 kPa total pressure, 12.2 mol Mo·s (mol CH<sub>4</sub>).

# Section S6. Supplemental discussion on benzene diffusion through CHA 8-MR windows and estimates of Weisz-Prater criterion

# 6.1 Supplemental discussion on zeolite flexibility

The 8-MR window size of 0.38 nm for CHA zeolite is determined assuming a rigid zeolite framework. Zeolite frameworks, however, have been observed to be "flexible", meaning that the zeolite lattice parameters (e.g., cell parameter, ring aperture) can expand or contract depending on temperature, pressure, and the presence of guest cations. 10-12 Accounting for "flexibility" in molecular dynamics simulations influence theoretical diffusion coefficient values as demonstrated by Demontis et al. 13 and Ermoshin and Engel 14 who reported that calculated methane diffusion coefficients increase when using a flexible MFI framework compared to a rigid structure. Crystal dynamic simulations by Deem et al. 15 also show the effect of temperature on zeolite (RHO, MFI, TON) pore size fluctuation, but also report that the extent of such fluctuations depend on the type of zeolite framework. Zeolite flexibility has been observed experimentally using, for example, neutron powder diffraction reporting zeolite cell expansion and change in ellipticity with increasing temperature. 16 Importantly, these theoretical and experimental studies allow rationalizing the diffusion of molecules larger than the size of zeolite pores and rings.

For example, Barrer and Vaughan reported measured uptakes at 540–720 K of Ar and Kr, with critical diameters of 0.33 and 0.36 nm, respectively, into the SOD zeolite that has a rigid pore diameter of 0.24 nm. <sup>17</sup> Another example is the diffusion of bulky molecules such as 1,3,5-tri-iso-propyl-benzene (critical diameter ~0.95 nm) and 1,3,5-tri-methylbenzene (critical diameter ~0.84 nm) into FAU zeolites that have a pore opening of ~0.74 nm, <sup>18–21</sup> performed at a wide range of temperature (298–600 K). Recently, it has been experimentally shown the uptake of iso-butane (kinetic diameter ~0.52 nm)<sup>22</sup> and benzene<sup>23</sup> into CHA zeolites at 303 K, albeit at a much slower

rate; equilibrium was not reached even after 1 h. Taken together, these studies demonstrate the diffusion of molecules that are greater in size compared to zeolite pore aperture.

### 6.2 Estimation of benzene diffusion coefficient in CHA zeolites

As described by Moore et al., the diffusion coefficient and rates decrease exponentially with increasing molecule diameter, revealing the activated process nature where molecules must overcome a barrier to diffuse from its equilibrium state.<sup>21</sup> Assuming that the diffusion of molecules through zeolites is an activated process we can relate the diffusion coefficient to its activation diffusion energy using an Eyring equation (or hop lattice equation)<sup>12,24</sup>:

$$D = \frac{l^2 k_B T}{h} \exp\left(\frac{-E_A}{RT}\right) \tag{S17}$$

where l is the lattice parameter,  $k_B$  is Boltzmann's constant, h is Planck's constant, T is temperature, R is the ideal gas constant, and  $E_A$  is the activation diffusion barrier. We can estimate the diffusion coefficient for benzene at our reaction temperature (950 K) using our DFT-calculated barrier of 184 kJ mol<sup>-1</sup>. The estimated diffusion coefficient is in the order of  $10^{-15}$  m<sup>2</sup> s<sup>-1</sup>, which is comparable to the experimental diffusion coefficient of *ortho*-xylene in MFI zeolites at 373 K determined from uptake experiments by Lercher and coworkers, <sup>25</sup> and diffusion coefficients for *meta*- and *ortho*-xylene using DFT-calculated barriers in MFI straight and sinusoidal channels at 373 K (Table S3).<sup>26</sup>

Table S3. Diffusion coefficients for benzene in CHA zeolites and xylene isomers in MFI

Molecule/Zeolite	$D_e^a / m^2 s^{-1}$
benzene/CHA	$^{ m a}3  imes 10^{-15}$
ortho-xylene/MFI	$^{\mathrm{b}}6.5 \times 10^{-18}$
meta-xylene/MFI	$^{\rm b}7 \times 10^{-19}$
ortho-xylene/MFI	$^{c}1.1 \times 10^{-16}$ ; $^{d}1.1 \times 10^{-23}$
meta-xylene/MFI	$^{c}5.1 \times 10^{-17}$ ; $^{d}4.5 \times 10^{-21}$

<sup>&</sup>lt;sup>a</sup>Estimated at 950 K using DFT-calculated diffusion barrier; <sup>b</sup>Determined experimentally at 373 K;<sup>25 c</sup>Determined using DFT-calculated diffusion barriers at 373 K in MFI straight channels.<sup>26</sup> Determined using DFT-calculated diffusion barriers at 373 K in MFI sinusoidal channels.<sup>26</sup>

#### 6.3 Weisz-Prater criterion

The Weisz-Prater (WP) criterion<sup>27</sup> was used to estimate the extent of zeolite intra-particle diffusion limitations on measured benzene formation rates. The criterion is defined as:

$$\frac{R_v r_p^2}{C_{Renzene} D_e} \le 1 \tag{S18}$$

where  $R_v$  is the rate of benzene formation per unit volume of catalyst,  $r_p$  is the crystallite radius,  $C_{Benzene}$  is the fluid-concentration of benzene, and  $D_e$  is the effective diffusivity of benzene. For Mo-MFI, we calculated  $R_v$  and  $C_{Benzene}$  using the benzene formation forward rate from our previous work.<sup>6</sup> To calculate  $C_{Benzene}$ , we averaged the benzene outlet pressure measured during deactivation until CH<sub>4</sub> conversion was below ~2.5%, above which point Razdan et al. showed that the benzene forward formation rate (per Mo) is invariant with conversion<sup>28</sup>. The effective diffusivity for benzene was obtained from Gobin et al. that was determined from frequency response experiments at 343 K in H-MFI zeolites with Si/Al ~45<sup>29</sup>. The diffusivity at 950 K was estimated using a lattice hop model equation (S18):

$$D_e(T_2) = D_e(T_1) * \frac{T_2}{T_1} \exp\left(-\frac{E_A}{R} \left(\frac{1}{T_2} - \frac{1}{T_1}\right)\right)$$
 (S19)

where  $D_e(T_1)$  is the effective diffusivity at 343 K and  $E_A$  is the apparent activation energy for diffusion reported by Gobin et al.<sup>29</sup> Moreover, the crystallite radius of H-MFI zeolites was obtained from Bickel et al. (CBV 2314; Zeolyst), that used the same parent zeolite used in our previous work.<sup>6,30</sup> We further estimated the WP for Mo-CHA catalysts, by using the same  $R_v$  used for Mo-MFI, assuming the active sites formed in Mo-CHA are similar in nature and reactivity compared to Mo-MFI. The effective diffusivity at 950 Kwas estimated using a hop lattice model and the diffusion barrier calculated using DFT (see Section 6.2).

Results for both Mo-MFI and Mo-CHA are shown in Table S4 and shows that measured rates of formation are limited by product mass transfer limitations to a greater extent in Mo-CHA compared to Mo-MFI catalysts.

**Table S4.** Weisz-Prater criterion estimates for Mo-zeolites at 950 K.

Catalyst	Crystallite Length / μm	$D_e^a / m^2 s^{-1}$	WP
Mo-MFI	0.30	$4.8 \times 10^{-11}$	$4 \times 10^{-4}$
Mo-CHA	0.50	$3 \times 10^{-15}$	$2 \times 10^{1}$
Mo-nanosheet-CHA	0.010	$3 \times 10^{-15}$	$0.5 \times 10^{1}$
<sup>a</sup> Estimated at 950 K			

# Section S7. Characterization of CHA zeolites with varying crystallite size

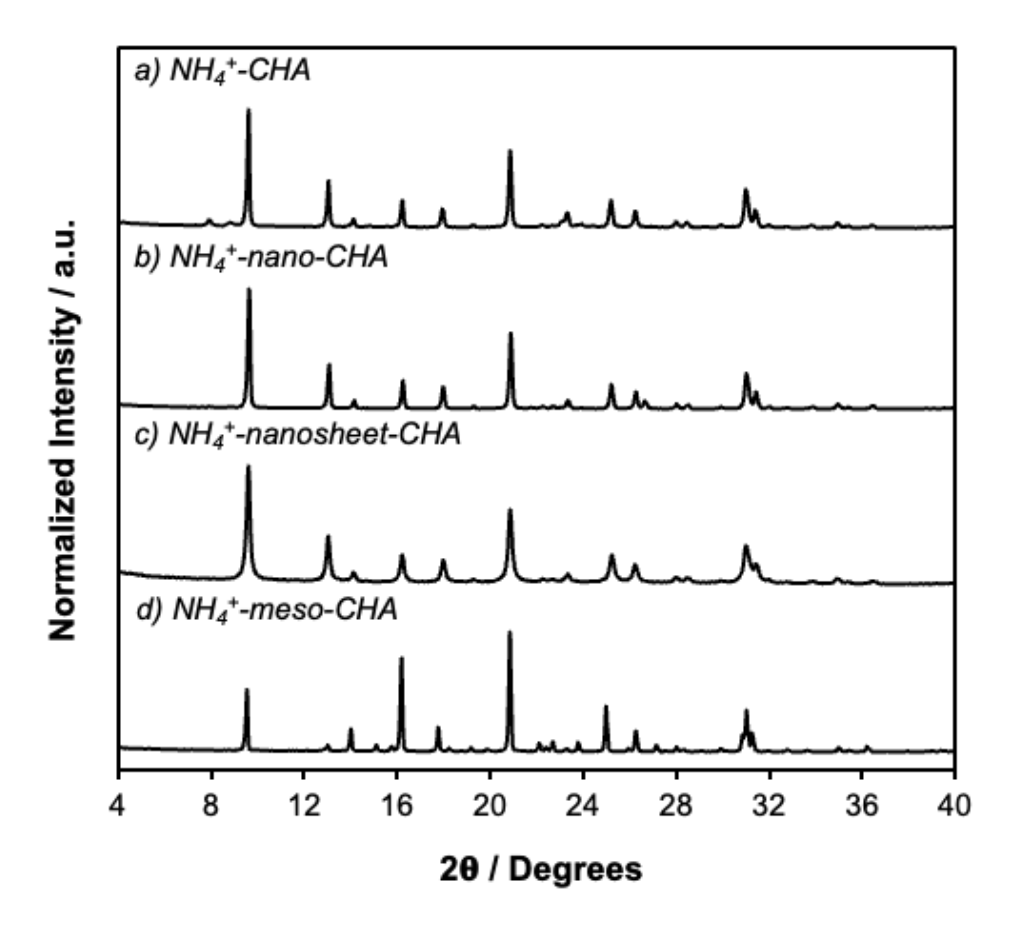


**Figure S14.** Powder XRD of a)  $NH_4^+$ -CHA b)  $NH_4^+$ -nano-CHA, c)  $NH_4^+$ -nanosheet-CHA, and d)  $NH_4^+$ -meso-CHA.

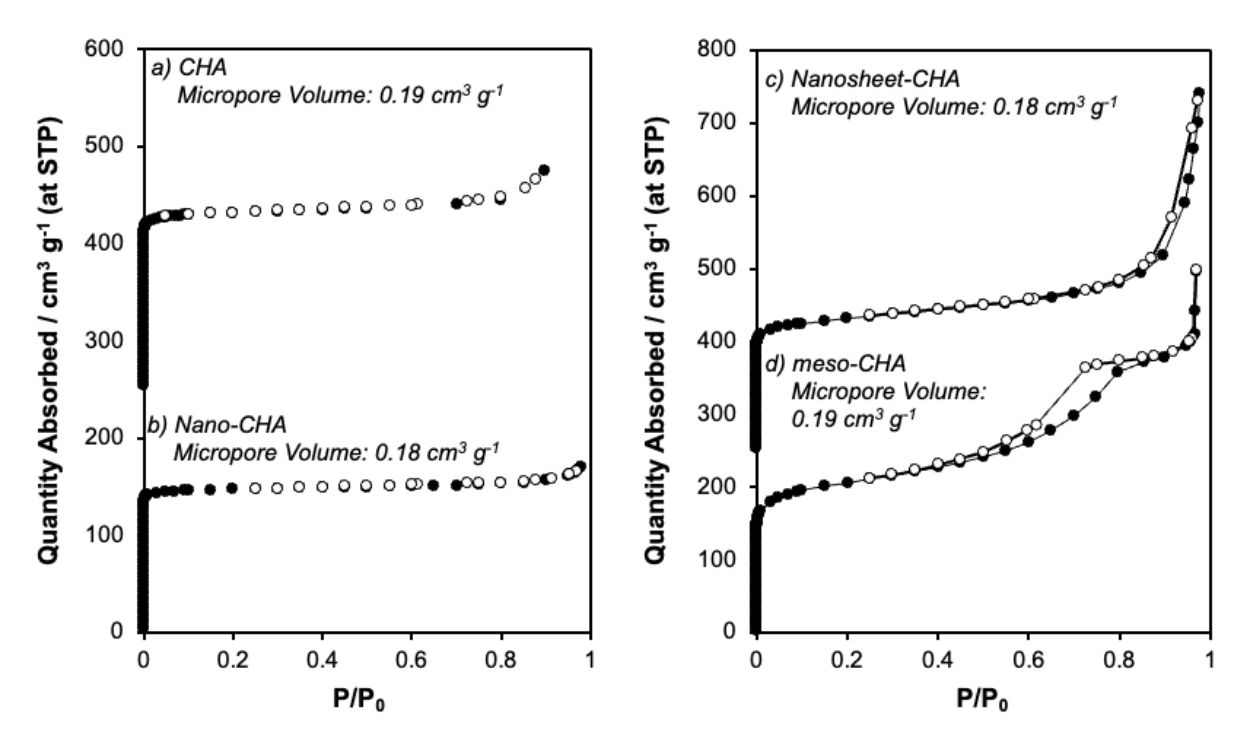


**Figure S15.** Ar adsorption (•) and desorption (○) isotherms (87 K) of a) CHA, b) Nano-CHA, c) Nanosheet-CHA, and d) Meso-CHA. Isotherms are vertically offset for clarity.

The XRD peak at ~9.60 20 of nanosheet-CHA and CHA synthesized without surfactant are compared in Figure S16 where significant peak broadening was observed, evincing the smaller crystallite size of nanosheet-CHA according to the Scherer equation, where peak width is inversely proportional to crystallite size. Determination of crystallite size, however, was not estimated from XRD since it has been demonstrated that strain- and instrument-induced broadening leads to underestimation (by a factor >2) of crystallites that are greater than 1  $\mu$ m.<sup>31</sup>

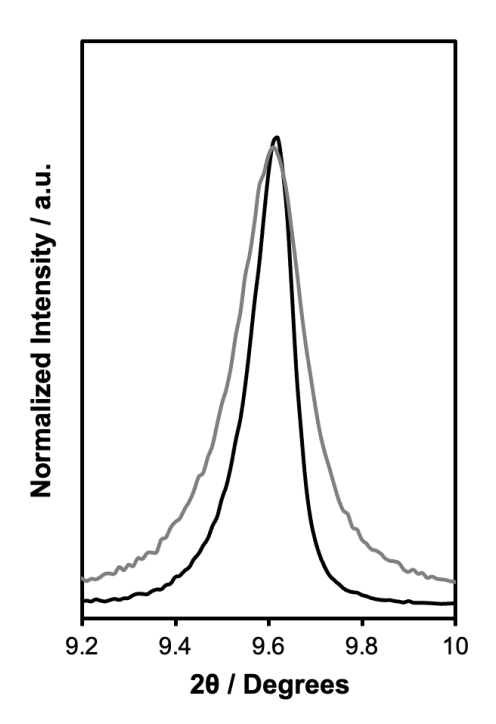


**Figure S16.** XRD peak at  $2\theta \sim 9.6^{\circ}$  of CHA (black trace) and nanosheet-CHA (grey trace).

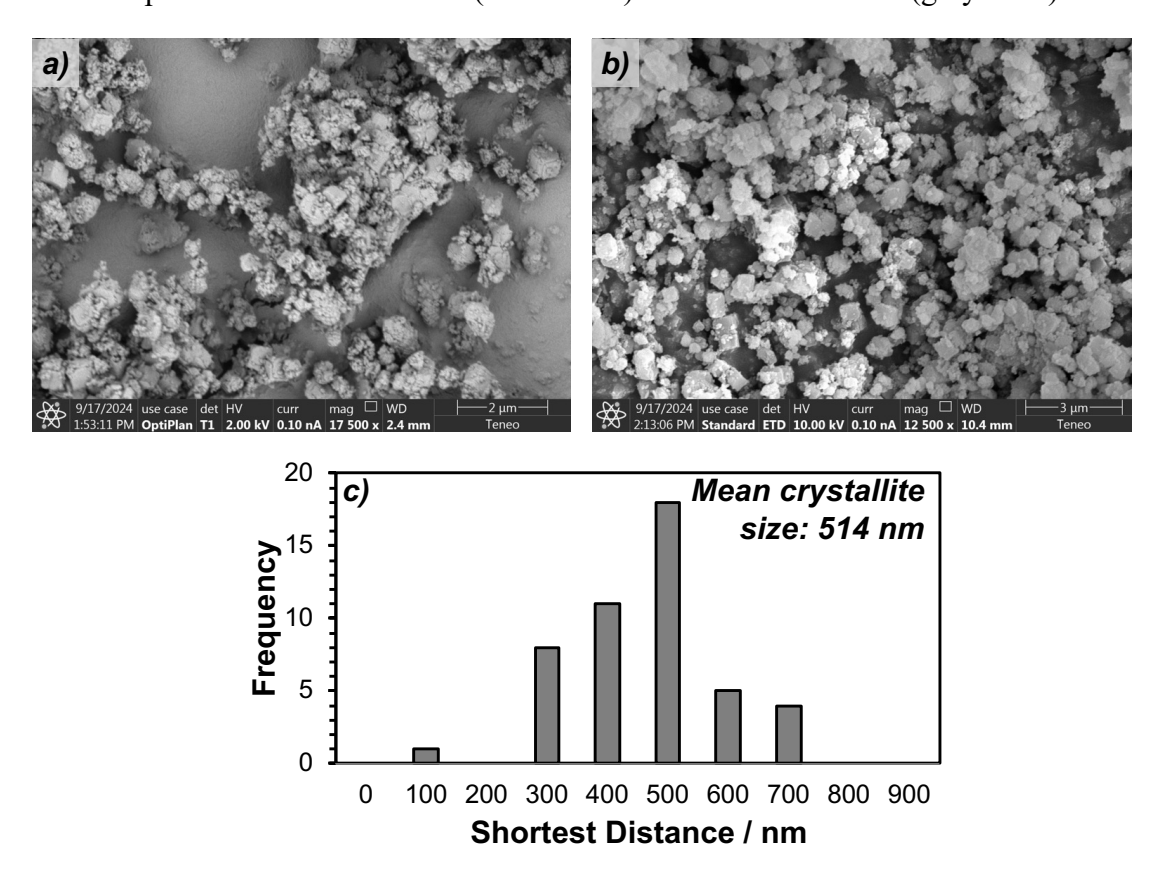


**Figure S17.** SEM images of Al-CHA at different magnifications (a,b) and c) crystallite size distribution obtained using (b).

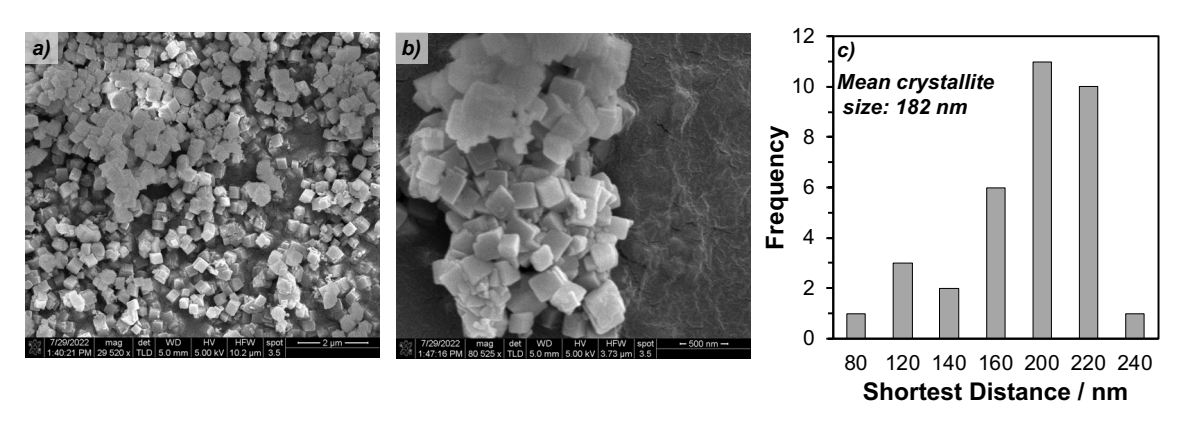


**Figure S18.** SEM images of nano-CHA at different magnifications (a,b) and c) crystallite size distribution obtained using (a).

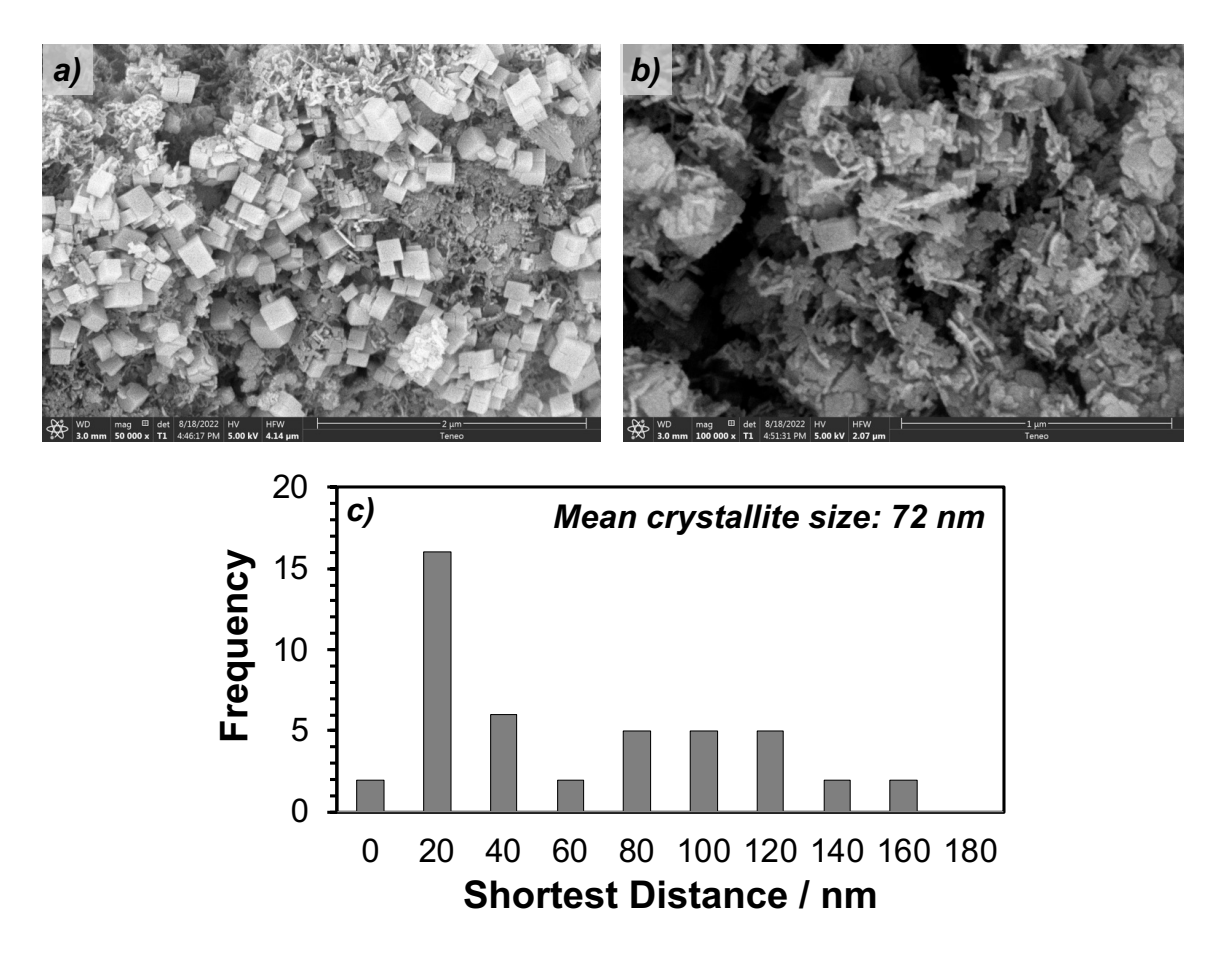


**Figure S19.** SEM images of nanosheet-CHA at different magnifications (a,b) and c) crystallite size distribution obtained using (a).

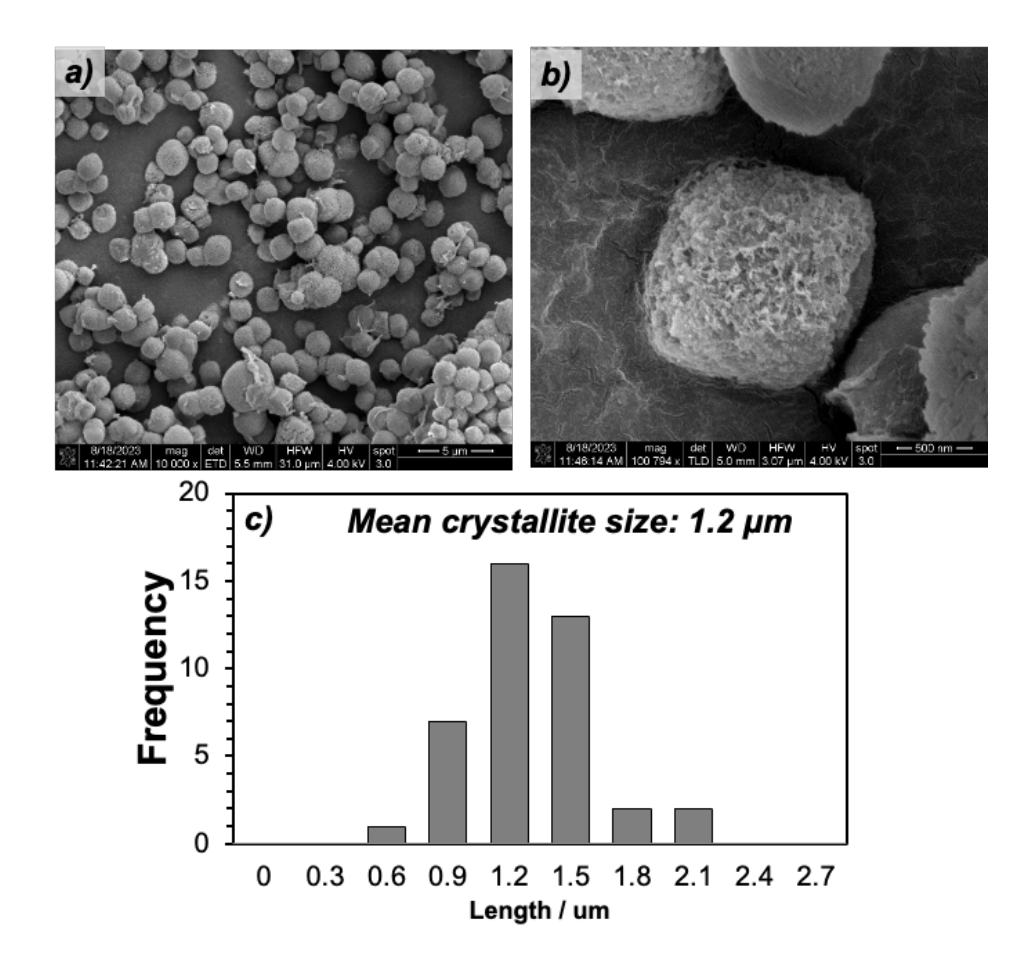


**Figure S20.** SEM images of meso-CHA at different magnifications (a,b) and c) crystallite size distribution obtained using (a).

Zeolite Brønsted acid sites (i.e., H<sup>+</sup> site) density was quantified using NH<sub>3</sub> temperature programmed desorption (TPD) that shows a single desorption peak (Supplementary Figure 21) corresponding to ammonia desorbed from H<sup>+</sup> sites.

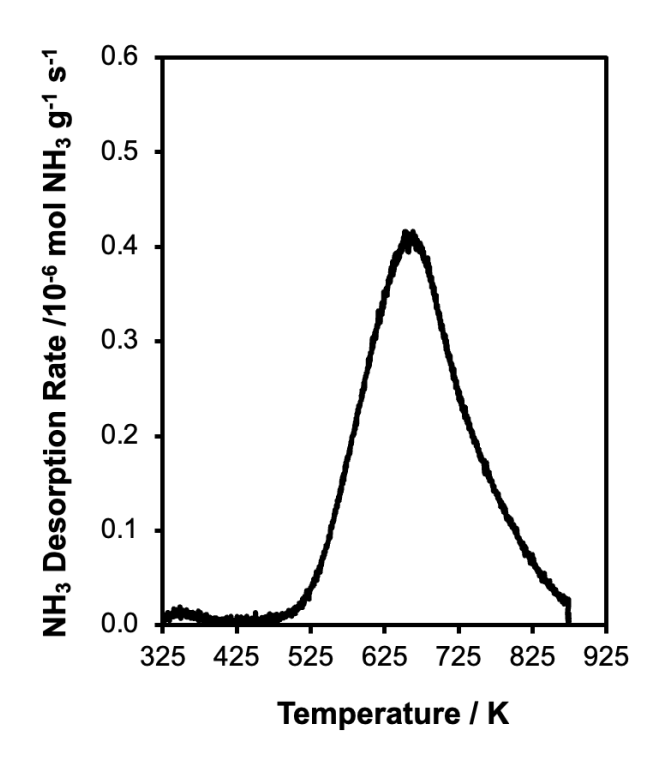


Figure S21. Representative NH<sub>3</sub> temperature programmed desorption profile of nanosheet-CHA.

**Table S5.** Elemental analysis and H<sup>+</sup> site density of CHA zeolites with varying crystallite size and mesoporous CHA.

Zeolite	Si/Al	H <sup>+</sup> /Al <sup>a</sup>
CHA	14.3	0.65
Nano-CHA	15	0.61
Nanosheet-CHA	15	0.58
Meso-CHA	20	0.52

 $^a$ Si/Al was determined with ICP-OES.  $^b$  H $^+$ /Al was quantified by NH $_3$  (H $^+$  sites) gas titration and ICP-OES (Al content).

**Table S6.** Elemental analysis of Mo supported on MFI, CHA zeolites with varying crystallite size and, mesoporous CHA.

Catalyst	Mo wt.%a	Mo/Al <sup>a</sup>	Residual H <sup>+</sup> /Al <sup>c</sup>
Mo-CHA	2.81	0.32	0.15
Mo-nano-CHA	2.46	0.29	-
Mo-nanosheet-CHA	2.79	0.30	0.23
Mo-meso-CHA	1.95	0.18	-
Mo-MFI <sup>b</sup>	1.90	0.15	-

<sup>&</sup>lt;sup>a</sup>Determined by ICP-OES; <sup>b</sup>Commercial MFI (CBV 2314; Si/Al = 11.5);  $^{c}H^{+}/Al$  was quantified by NH<sub>3</sub> (H<sup>+</sup> sites) gas titration and ICP-OES (Al content).

# Section S8. Influence of zeolite support topology on product selectivity during methane DHA

Zhang et al. studied the influence of zeolite topology (MFI, FAU, CHA (SAPO-34)) on methane DHA conversion and benzene selectivity, reporting that coke selectivity was higher for FAU and CHA than MFI,<sup>32</sup> attributing higher coke selectivity on Mo-FAU to the presence of large cages (~1.1 nm) promoting aromatic ring condensation, but rationalizing low aromatics yields on Mo-CHA to be hindered by diffusional restrictions imposed by its small pores. Our data show that benzene rates (and yields) increase with decreasing CHA crystallite size, and are higher on mesoporous CHA than Mo-CHA. Coke selectivity decreases slightly on Mo-nanosheet-CHA and Mo-mesoporous CHA, relative to Mo-CHA, which is consistent with decreasing intraparticle residence time of aromatic compounds that would limit the extent of polyaromatic reactions to form coke. (Fig. 3b). We hypothesize that, similar to Mo-FAU, formation of polyaromatic carbonaceous deposits in the cage-like cavities of CHA (~0.74 nm) that are larger than the largest void in MFI (~0.64 nm) is favored, leading to higher cumulative carbon selectivity in CHA.

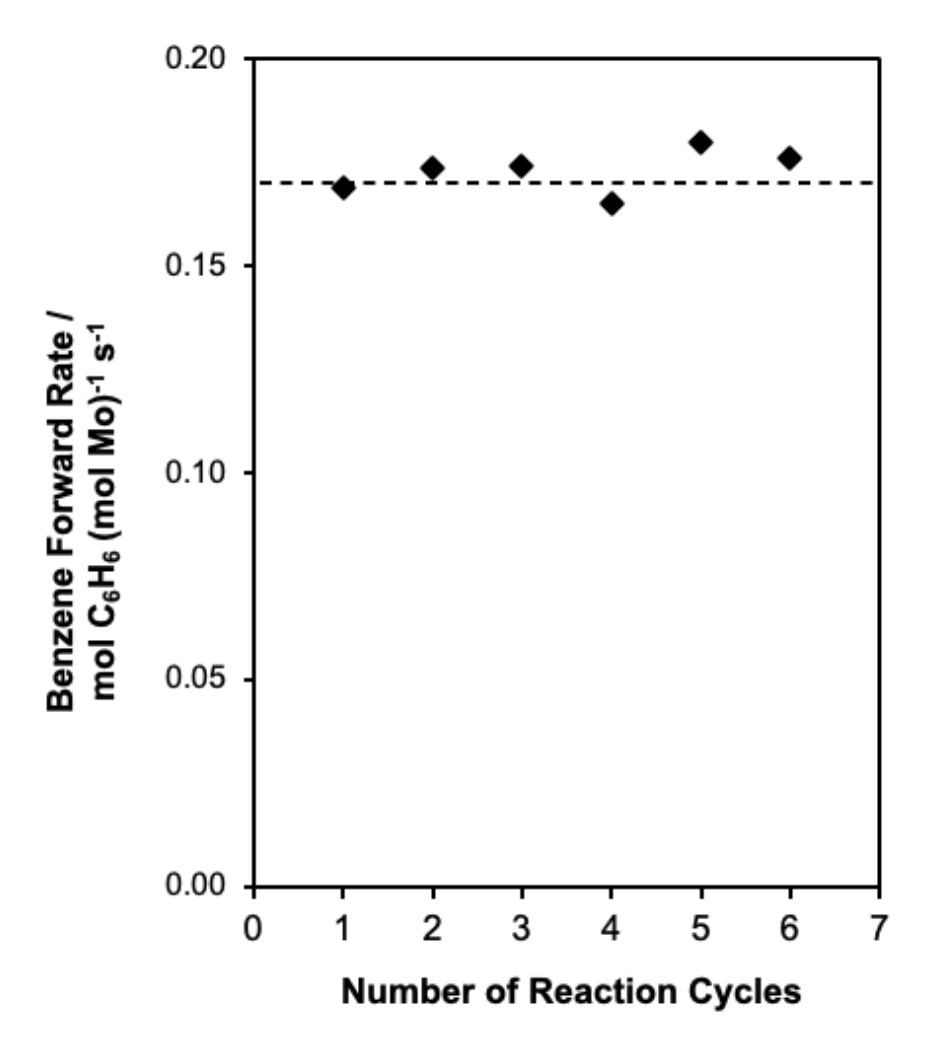


**Figure S22.** Benzene forward rate measured on Mo-meso-CHA during consecutive methane DHA reaction-regeneration cycles. Reaction conditions: 950 K, 90 kPa CH<sub>4</sub>. Regeneration conditions: 823 K, 20 kPa O<sub>2</sub>, 6 h.

# Section S10. Characterization of Mo-Zeolites before and after DHA reaction-regeneration cycles

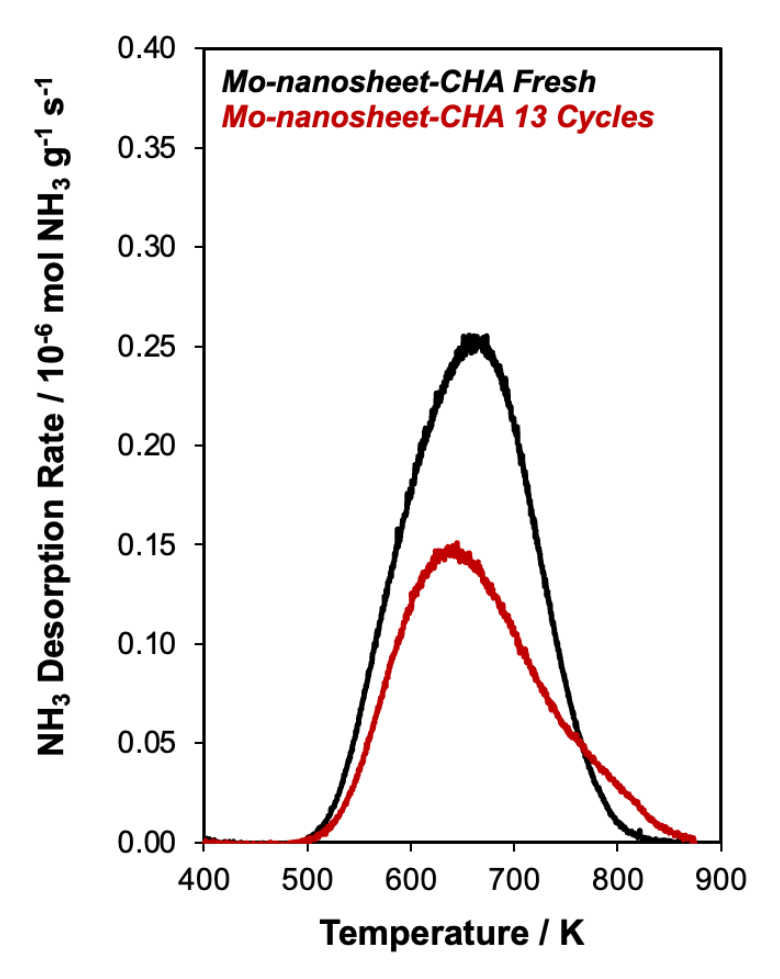


**Figure S23.** NH<sub>3</sub> desorption profiles for residual H<sup>+</sup> sites in Mo-nanosheet-CHA fresh (black trace) and Mo-nanosheet-CHA after 13 cycles of reaction-regeneration (red trace).

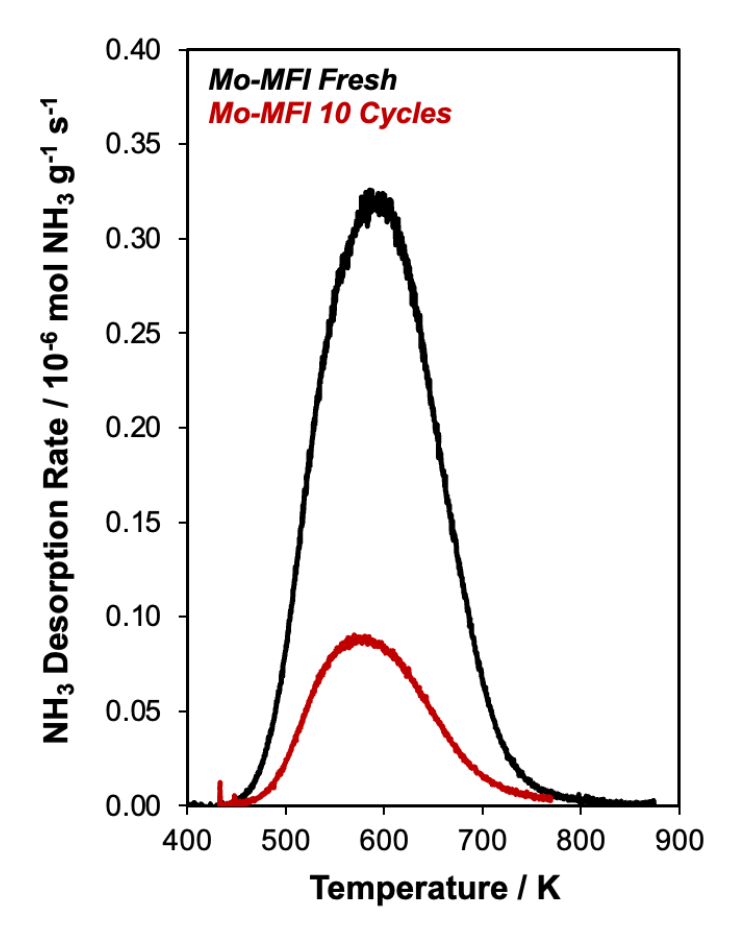


**Figure S24.** NH<sub>3</sub> desorption profiles for residual H<sup>+</sup> sites in Mo-MFI fresh (black trace) and Mo-MFI after 10 cycles of reaction-regeneration (red trace) adapted from Santiago-Colón and Gounder<sup>6</sup> Copyright 2024 Journal of Catalysis.

**Table S7.** Quantification of residual H<sup>+</sup> site density normalized per Al (H<sup>+</sup>/Al) on Mo-Zeolites before and after reaction-regeneration samples.

Catalyst	Residual H <sup>+</sup> /Al before DHA	Residual H <sup>+</sup> /Al after DHA cycles	
	cycles		
Mo-MFI	0.20	$0.05^{\rm b}$	
Mo-nanosheet-CHA	0.23	0.15	
*Determined by ICD OES, had dented from Sentiage Colon and Counder Converient 2024 Journal of			

<sup>&</sup>lt;sup>a</sup>Determined by ICP-OES; <sup>b</sup>Adapted from Santiago-Colón and Gounder Copyright 2024 Journal of Catalysis.

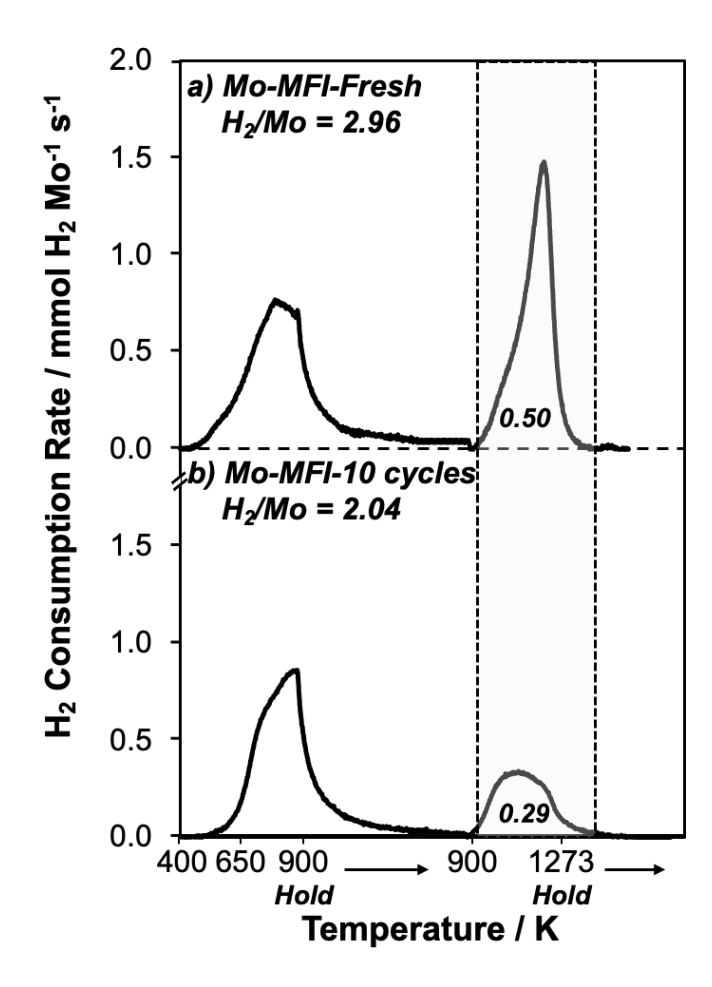


**Figure S25.** H<sub>2</sub> TPR profiles of a) fresh Mo-MFI and b) Mo-MFI after 10 cycles of reaction and regeneration. Total H<sub>2</sub> consumed (per Mo) and fraction of H<sub>2</sub> consumed in the high-temperature feature per (~1260 K, grey square) total H<sub>2</sub> consumed are shown inside the profile. Data reproduced from Santiago-Colón and Gounder<sup>6</sup> Copyright 2024 Journal of Catalysis.<sup>6</sup>

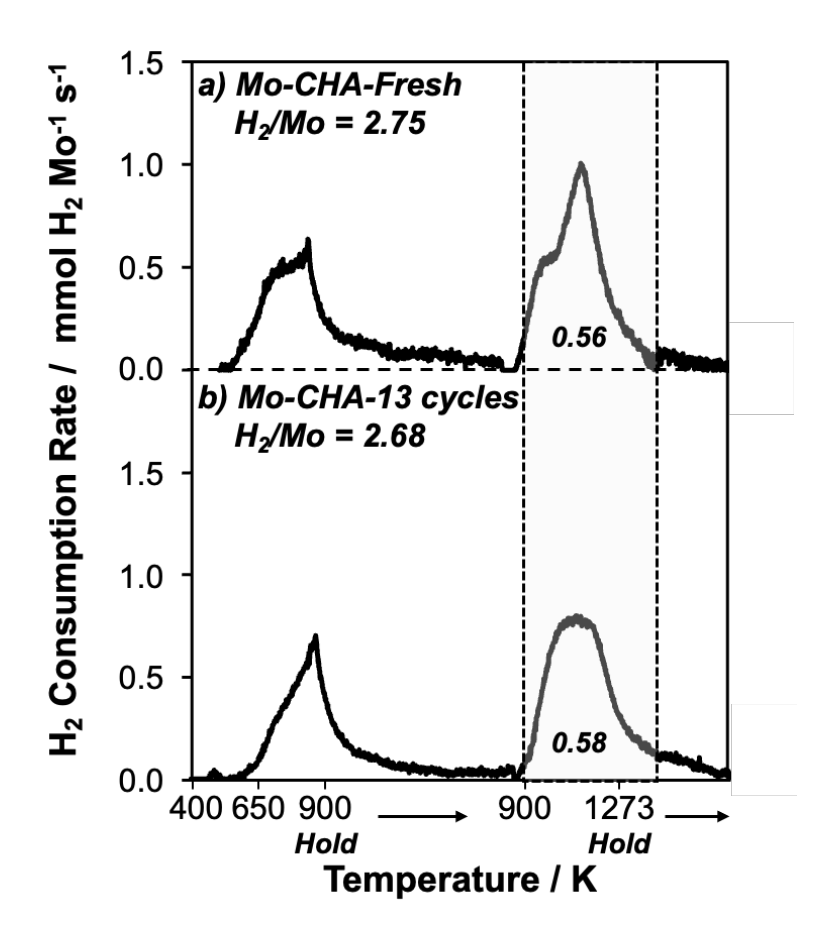


**Figure S26.** H<sub>2</sub> TPR profiles of a) fresh Mo-nanosheet-CHA and b) Mo-nanosheet-CHA after 13 cycles of reaction and regeneration. Total H<sub>2</sub> consumed (per Mo) and fraction of H<sub>2</sub> consumed in the high-temperature feature per (~1260 K, grey square) total H<sub>2</sub> consumed are shown inside the profile.

# Section S11. High resolution transmission electron microscopy

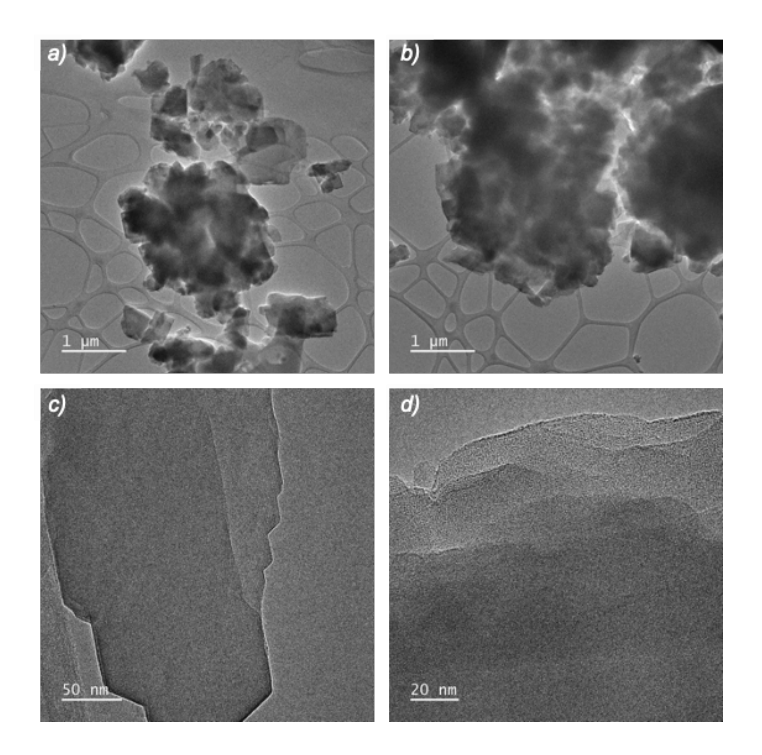


**Figure S27.** (a-d) High-resolution TEM images of Mo-MFI at various magnifications and on different particles before reaction-regeneration cycles (fresh catalyst).

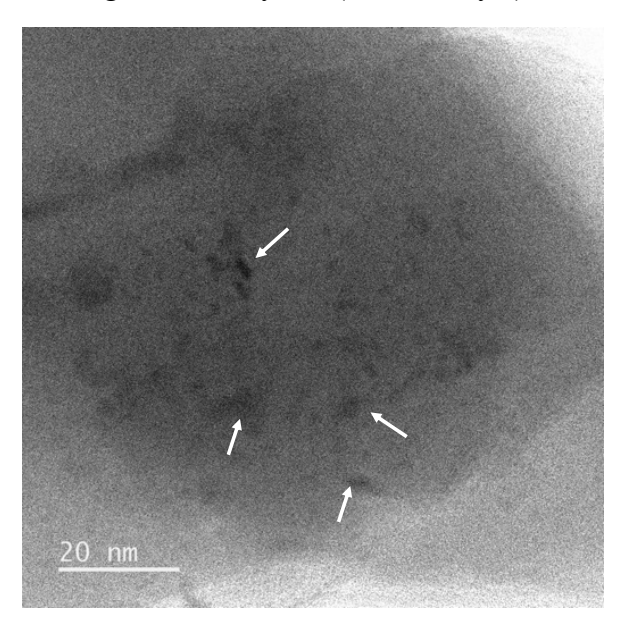


**Figure S28.** Annular bright field STEM image of Mo-MFI after 10 reaction-regeneration cycles (spent catalyst). White arrows point to dark spots corresponding to Mo agglomerates formed during reaction-regeneration cycles.

## Section S12. Characterization of RTH and AEI zeolites

Powder XRD patterns were collected on synthesized RTH (Figure S29b) and AEI zeolites (Figure S30) and show characteristic peaks corresponding to the RTH and AEI framework. XRD are compared to the theoretical pattern obtained from the International Zeolite Association (IZA).

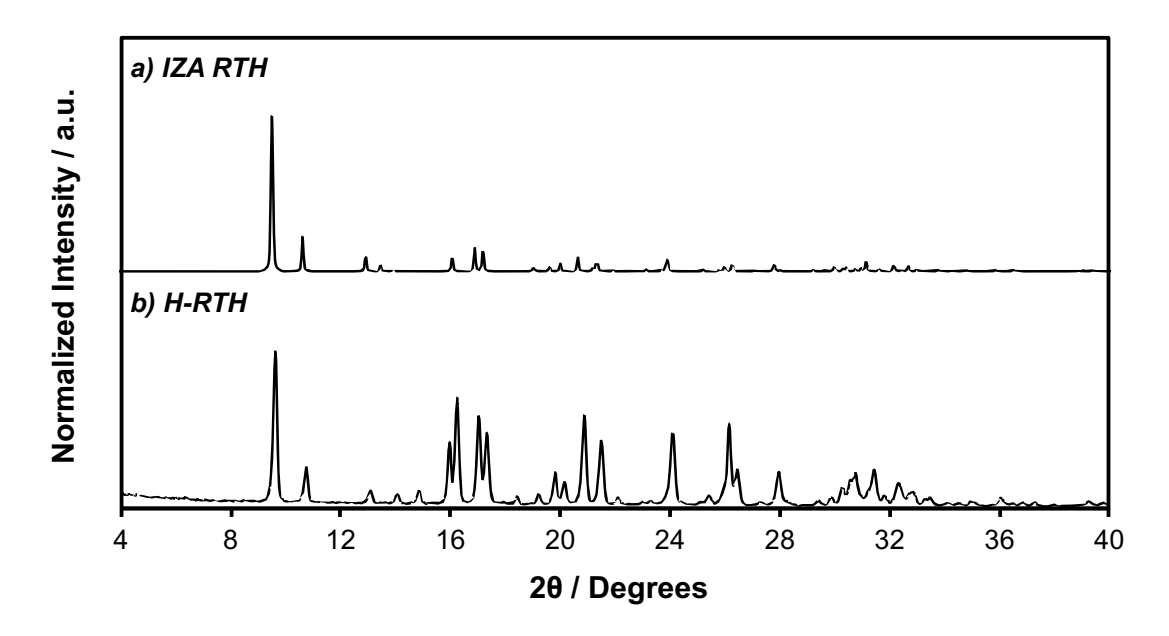


Figure S29. Powder XRD of a) RTH from IZA (calculated) and b) synthesized H-RTH.

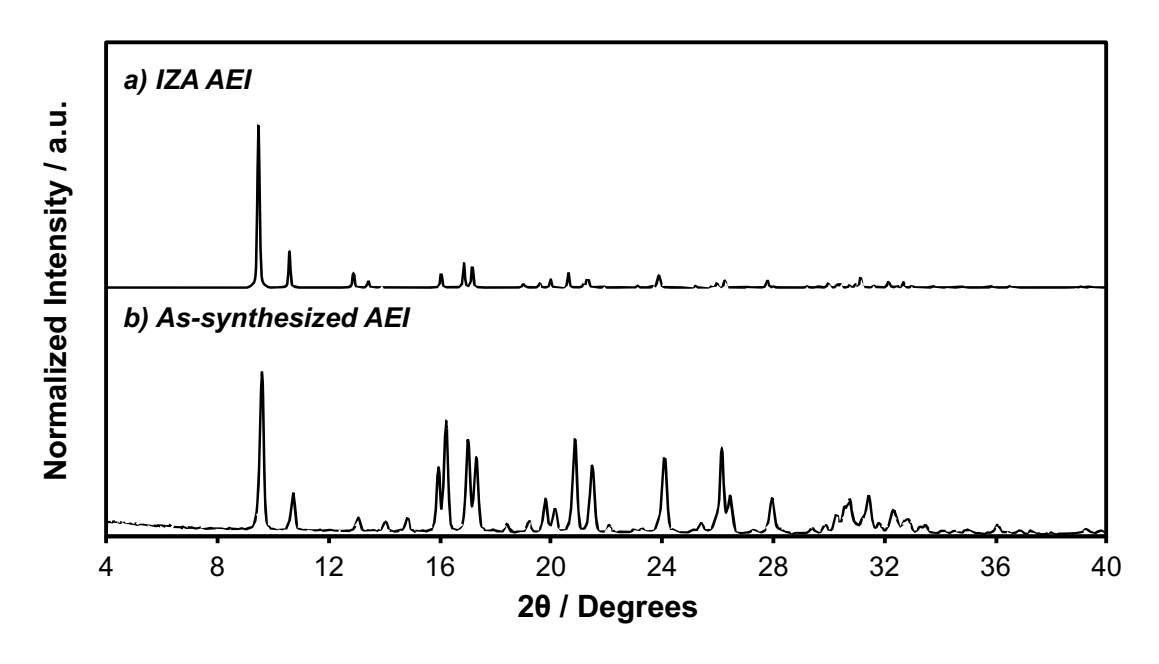


Figure S30. Powder XRD of a) AEI from IZA (calculated) and b) as-synthesized AEI zeolite.

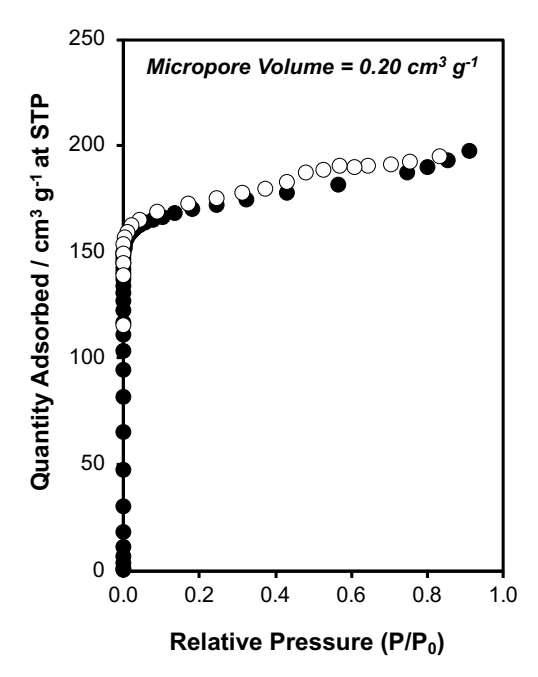


Figure S31. Ar isotherm adsorption (black circles) and desorption (open circles) of H-RTH.

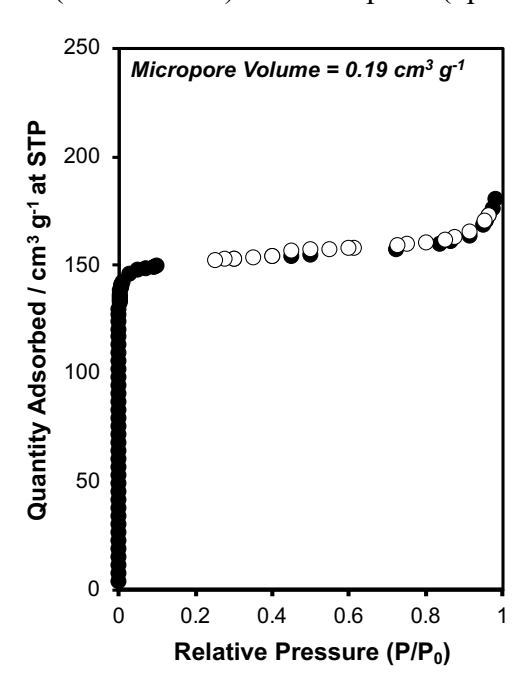


Figure S32. Ar isotherm adsorption (black circles) and desorption (open circles) of H-AEI.

**Table S8.** Elemental analysis of Mo-RTH after high-temperature air treatment.

Sample	Si/Al	Mo/Al	Mo wt.%
Mo-RTH	13.2	0.28	2.65
Mo-AEI	7.3	0.20	2.99

# Section S13. Methane DHA kinetic data on Mo-RTH and Mo-AEI zeolites

Benzene forward formation rates (per Mo; 950 K, 90 kPa CH<sub>4</sub>) as a function of time-on-stream measured on Mo-RTH and Mo-AEI are shown in Figure S33 and Figure S34, respectively. Initial forward rates are lower compared to Mo-CHA (~3.5x for Mo-RTH and ~1.5x for Mo-AEI).

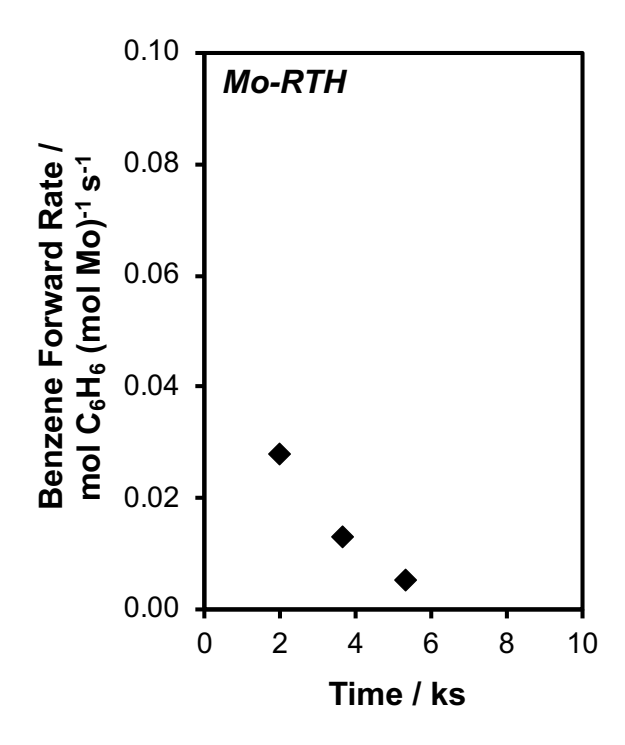


**Figure S33.** Benzene forward rate measured on Mo-RTH. Reaction conditions: 950 K, 90 kPa CH<sub>4</sub>, 105 kPa.

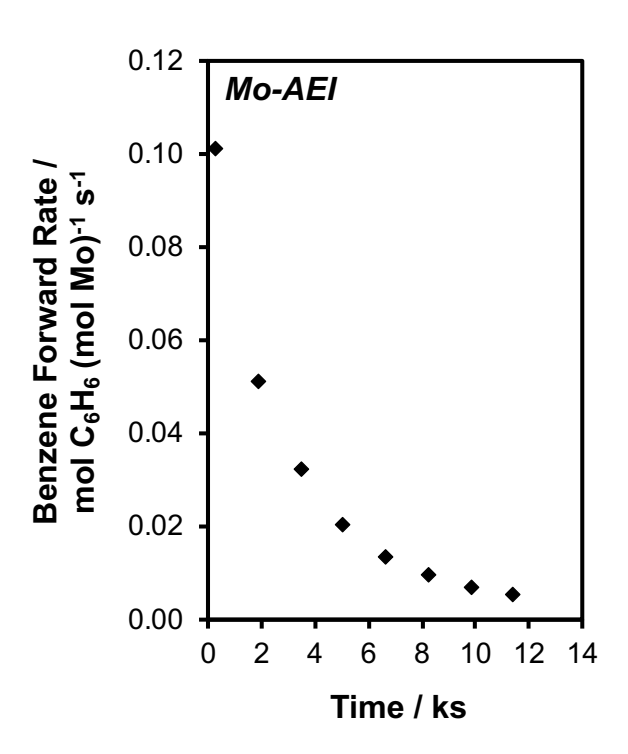


**Figure S34.** Benzene forward rate measured on Mo-AEI. Reaction conditions:  $950 \, \text{K}$ ,  $90 \, \text{kPa CH}_4$ ,  $105 \, \text{kPa}$ .

#### References

- (1) Iorio, J. R. Di; Gounder, R. Controlling the Isolation and Pairing of Aluminum in Chabazite Zeolites Using Mixtures of Organic and Inorganic Structure-Directing Agents. *Chemistry of Materials* **2016**, *28* (7), 2236–2247. https://doi.org/10.1021/ACS.CHEMMATER.6B00181.
- (2) Kumar, M.; Luo, H.; Románromán-Leshkov, Y.; Rimer, J. D. SSZ-13 Crystallization by Particle Attachment and Deterministic Pathways to Crystal Size Control. *J. Am. Chem. Soc* **2015**, *137*, 13007–13017. https://doi.org/10.1021/jacs.5b07477.
- (3) Santiago-Colón, Á.; Lee, S.; Gounder, R. Method for Making CHA Zeolites and Zeotypes. US 63/529264, July 2024.
- (4) Schmidt, J. E.; Deimund, M. A.; Davis, M. E. Facile Preparation of Aluminosilicate RTH across a Wide Composition Range Using a New Organic Structure-Directing Agent. *Chemistry of Materials* **2014**, *26* (24), 7099–7105. https://doi.org/10.1021/CM503625U.
- (5) Boruntea, C. R.; Lundegaard, L. F.; Corma, A.; Vennestrøm, P. N. R. Crystallization of AEI and AFX Zeolites through Zeolite-to-Zeolite Transformations. *Microporous and Mesoporous Materials* **2019**, *278*, 105–114. https://doi.org/10.1016/j.micromeso.2018.11.002.
- (6) Santiago-Colón, Á. N.; Gounder, R. Structural Changes to Molybdenum and Brønsted Acid Sites in MFI Zeolites during Methane Dehydroaromatization Reaction-Regeneration Cycles. *J Catal* **2024**, *430*, 115335. https://doi.org/10.1016/j.jcat.2024.115335.
- (7) Leshchev, D.; Rakitin, M.; Luvizotto, B.; Kadyrov, R.; Ravel, B.; Attenkofer, K.; Stavitski, E. The Inner Shell Spectroscopy Beamline at NSLS-II: A Facility for in Situ and Operando X-Ray Absorption Spectroscopy for Materials Research. *J Synchrotron Radiat* **2022**, *29*, 1095–1106. https://doi.org/10.1107/S160057752200460X.
- (8) Razdan, N. K.; Kumar, A.; Foley, B. L.; Bhan, A. Influence of Ethylene and Acetylene on the Rate and Reversibility of Methane Dehydroaromatization on Mo/H-ZSM-5 Catalysts. *J Catal* **2020**, *381*, 261–270. https://doi.org/10.1016/j.jcat.2019.11.004.
- (9) Bedard, J.; Hong, D. Y.; Bhan, A. CH4 Dehydroaromatization on Mo/H-ZSM-5: 1. Effects of Co-Processing H2 and CH3COOH. *J Catal* **2013**, *306*, 58–67. https://doi.org/10.1016/j.jcat.2013.06.003.
- (10) Smit, B.; Maesen, T. L. M. Molecular Simulations of Zeolites: Adsorption, Diffusion, and Shape Selectivity. *Chem Rev* **2008**, *108* (10), 4125–4184. https://doi.org/10.1021/cr8002642.
- (11) Ghojavand, S.; Dib, E.; Mintova, S. Flexibility in Zeolites: Origin, Limits, and Evaluation. *Chem Sci* **2023**, *14* (44), 12430–12446. https://doi.org/10.1039/d3sc03934j.

- (12) Xiao, J.; Wei, J. Diffusion Mechanism of Hydrocarbons in Zeolite-I. Theory. *Chem Eng Sci* **1992**, *47* (5), 1123–1141.
- (13) Demontis, P.; Fois, E.; Suffritti, G. Molecular Dynamics Studies on Zeolites. 4. Diffusion of Methane in Silicalite. *Journal of Physical Chemistry* **1990**, *94* (23), 2850.
- (14) Ermoshin, V. A.; Engel, V. Construction of a Potential Energy Surface for Molecular Dynamics Studies of Methane Adsorbed in Zeolites. *Journal of Physical Chemistry A* **1999**, *103* (26), 5116–5122. https://doi.org/10.1021/jp9843860.
- (15) Deem, M.; Newsam, J.; Creighton, J. Fluctuations in Zeolite Aperture Dimensions Simulated by Crystal Dynamics. *J. Am. Chem. Soc* **1992**, *114*, 7198–7207.
- (16) Parise, J. B.; Abrams, L.; Gier, E.; Corbin, D. R.; Jorgensen, J. D.; Prince, E. Flexibility of the Framework of Zeolite Rho. Structural Variation from 11 to 573 K. A Study Using Neutron Powder Diffraction Data; 1984; Vol. 88. https://pubs.acs.org/sharingguidelines.
- (17) Barrer, R. M.; Vaugitan, D. E. W. Trapping of Inert Gases in Sodalite and Cancrinite Crystals. *J. Phys. Chem. Solids* **1971**, *32*, 731–743.
- (18) Al-Khattaf, S.; De Lasa, H. *The Role of Diffusion in Alkyl-Benzenes Catalytic Cracking*; 2002; Vol. 226.
- (19) Satterfield, C. N.; Cheng, C. S. Liquid Counterdiffusion of Selected Aromatic and Naphthenic Hydrocarbons in Type Y Zeolites. *AIChE Journal* **1972**, *18* (4), 724–728. https://doi.org/10.1002/aic.690180410.
- (20) Ruthven, D. M.; Kaul, B. K. *Adsorption of Aromatic Hydrocarbons in NaX Zeolite*. 2. *Kinetics*; 1993; Vol. 32. https://pubs.acs.org/sharingguidelines.
- (21) Moore, R. M.; Katzer, J. R. Counterdiffusion of Liquid Hydrocarbons in Type Y Zeolite: Effect of Molecular Size, Molecular Type, and Direction of Diffusion. *AIChE Journal* **1972**, *18* (4), 816–824. https://doi.org/10.1002/aic.690180426.
- (22) Zhu, X.; Hofmann, J. P.; Mezari, B.; Kosinov, N.; Wu, L.; Qian, Q.; Weckhuysen, B. M.; Asahina, S.; Ruiz-Martínez, J.; Hensen, E. J. M. Trimodal Porous Hierarchical SSZ-13 Zeolite with Improved Catalytic Performance in the Methanol-to-Olefins Reaction. ACS Catal 2016, 6 (4), 2163–2177. https://doi.org/10.1021/acscatal.5b02480.
- (23) Bolshakov, A.; Van Hoof, A. J. F.; Mezari, B.; Kosinov, N.; Hensen, E. A Versatile Mono-Quaternary Ammonium Salt as a Mesoporogen for the Synthesis of Hierarchical Zeolites. *Catal Sci Technol* **2019**, *9* (23), 6737–6748. https://doi.org/10.1039/c9cy02001b.
- (24) Smith, A. T.; Plessow, P. N.; Studt, F. Density Functional Theory Calculations of Diffusion Barriers of Organic Molecules through the 8-Ring of H-SSZ-13. *Chem Phys* **2021**, *541*, 111033. https://doi.org/10.1016/j.chemphys.2020.111033.
- (25) Mirth, G.; Cejka, J.; Lercher, J. Transport and Isomerization of Xylenes over HZSM-5 Zeolites. *J Catal* **1993**, *139*, 24–33.

- (26) DeLuca, M.; Hibbitts, D. Predicting Diffusion Barriers and Diffusivities of C6–C12 Methylbenzenes in MFI Zeolites. *Microporous and Mesoporous Materials* **2022**, 333. https://doi.org/10.1016/j.micromeso.2022.111705.
- (27) Weisz, P. B.; Prater, C. D. Interpretation of Measurements in Experimental Catalysis. In *Advances in Catalysis*; 1954; Vol. 6, pp 143–196.
- (28) Razdan, N. K.; Bhan, A. Carbidic Mo Is the Sole Kinetically-Relevant Active Site for Catalytic Methane Dehydroaromatization on Mo/H-ZSM-5. *J Catal* **2020**, *389*, 667–676. https://doi.org/10.1016/j.jcat.2020.06.035.
- (29) Gobin, O. C.; Reitmeier, S. J.; Jentys, A.; Lercher, J. A. Diffusion Pathways of Benzene, Toluene and p-Xylene in MFI. *Microporous and Mesoporous Materials* **2009**, *125* (1–2), 3–10. https://doi.org/10.1016/j.micromeso.2009.01.025.
- (30) Bickel, E. E.; Lee, S.; Gounder, R. Influence of Brønsted Acid-Site Density on Reaction-Diffusion Phenomena That Govern Propene Oligomerization Rate and Selectivity in MFI Zeolites. *ACS Catal* **2023**, *13* (2), 1257–1269. https://doi.org/10.1021/ACSCATAL.2C05184.
- (31) Burton, A. W.; Ong, K.; Rea, T.; Chan, I. Y. On the Estimation of Average Crystallite Size of Zeolites from the Scherrer Equation: A Critical Evaluation of Its Application to Zeolites with One-Dimensional Pore Systems. *Microporous and Mesoporous Materials* **2009**, *117* (1–2), 75–90. https://doi.org/10.1016/j.micromeso.2008.06.010.
- (32) Zhang, C.-L.; Li, S.; Yuan, Y.; Zhang, W.-X.; Wu, T.-H.; Lin, L.-W. Aromatization of Methane in the Absence of Oxygen over Mo-Based Catalysts Supported on Different Types of Zeolites. *Catal Letters* **1998**, *56*, 207–213.